Research Square

Preprints are preliminary reports that have not undergone peer review.
They should not be considered conclusive, used to inform clinical practice,
or referenced by the media as validated information.

Fluctuating conduit dynamics during the 877 CE Hrafntinnuhraun rhyolitic fissure eruption, Torfajökull, Iceland

Jingwei Zhang

j.zhang77@lancaster.ac.uk

Lancaster University

Alastair G. E. Hodgetts

University of Edinburgh

Marina Godbillot

Université Clermont Auvergne

Hugh Tuffen

Lancaster University

Dave McGarvie

Lancaster University

Fabian B. Wadsworth

Ludwig-Maximilians-Universität München

Jeremie Vasseur

Ludwig-Maximilians-Universität München

Corin Jorgenson

University of Strathclyde

Katherine J. Dobson

University of Strathclyde

Simon Falvard

Université Clermont Auvergne

Lucia Gurioli

Université Clermont Auvergne

Andrew Harris

Université Clermont Auvergne

Daníel Freyr Sigurbjargarson

Nature Conservation Agency of Iceland

Research Article

Keywords: silicic volcanism, explosive-effusive transition, cryptic fragmentation, rhyolite, sintering

Posted Date: September 29th, 2026

DOI: https://doi.org/10.21203/rs.3.rs-11012865/v1

License: This work is licensed under a Creative Commons Attribution 4.0 International License.
Read Full License

Additional Declarations: No competing interests reported.

Fluctuating conduit dynamics during the 877 CE Hrafntinnuhraun rhyolitic fissure eruption, Torfajökull, Iceland

Jingwei Zhang[1*], Alastair G. E. Hodgetts[2], Marina Godbillot[3], Hugh Tuffen[1], Dave McGarvie[1], Fabian B. Wadsworth[4], Jeremie Vasseur[4], Corin Jorgenson[5], Katherine J. Dobson[5], Simon Falvard[3], Lucia Gurioli[3], Andrew Harris[3], Daníel Freyr Sigurbjargarson[6]

[1*]Lancaster Environment Centre, Lancaster University, Lancaster, United Kingdom.
[2]School of GeoSciences, University of Edinburgh, Edinburgh, United Kingdom.
[3]Laboratoire Magmas et Volcans, Université Clermont Auvergne, CNRS, IRD, OPGC,Aubière, France.
[4]Department of Earth and Environmental Sciences, Ludwig-Maximilians-Universität München, Munich, Germany.
[5]Departments of Civil & Environmental Engineering and Chemical & Process Engineering, University of Strathclyde, Glasgow, United Kingdom.
[6]Nature Conservation Agency of Iceland, Hvolsvöllur, Iceland.

*Corresponding author(s). E-mail(s): j.zhang77@lancaster.ac.uk;

Abstract

The rhyolitic 877 CE Hrafntinnuhraun eruption at Torfajökull produced a widespread and important tephra layer (Landnám/Settlement Layer) and is a key example of a hybrid silicic eruption in Iceland. Despite this, its proximal pyroclastic deposits remain largely unstudied, leaving a gap in our understanding of the factors controlling the eruption and its evolution.

Here, we present the first detailed characterization of proximal HRN tephra, centered upon a 4.5 m-thick fall deposit located within 2 km of the source vent(s). We present deposit grain size and componentry, measurements of pyroclast H_2O

concentrations, major and trace element geochemistry, vesicle number density, and vesicle size distribution. Together, these data permit the reconstruction of shifting conduit processes during the recorded activity, which comprises vent opening, a first explosive phase, a lull/pause, vent reopening, pulsatory Vulcanian pulses, and final low-intensity phase that occurred alongside lava effusion.
Juvenile obsidians are interpreted to have been generated by sintering at the conduit walls, with ejection depths overall shallowing towards the surface as the intensity lessened. High pumice vesicle number densities are determined for three units and suggest that high magma decompression rates occurred throughout the eruption, even as it waned, and this may reflect abrupt, transient excavations of a narrowing conduit during Vulcanian explosions.
All evidence points towards a complex eruption with multiple phases of activity, and sets the scene for more detailed examination of both pyroclast texture and the depositional architecture of the tephra deposit of this significant silicic eruption of cross-disciplinary importance.

Keywords: silicic volcanism; explosive-effusive transition; cryptic fragmentation; rhyolite; sintering

1 Introduction

Explosive silicic eruptions are among the most hazardous geological events on Earth, yet they are rarely observed directly because of their infrequency (Cassidy et al. 2018) . The recent subaerial rhyolitic eruptions of Chaitén (2008–2009, Chile; Pallister et al. 2013; Watt et al. 2009) and Cordón Caulle (2011–2012, Chile; Elissondo et al. 2016) provided unprecedented observations of complex and highly unsteady eruptive behavior, with transitions occurring over timescales ranging from minutes to days (Schipper et al. 2013; Crozier et al. 2022). Both eruptions evolved from an initial Plinian-to-sub-Plinian phase, through pulsatory Vulcanian activity, to a hybrid state of simultaneous low-intensity ash venting and lava effusion (Schipper et al. 2021; Wadsworth et al. 2022). However, the mechanisms that govern the transition from the initial explosive phase to this hybrid explosive–effusive behavior remain poorly constrained, and it is unclear whether such transitions are characteristic of silicic systems more generally (Castro and Walter 2021; Trafton and Giachetti 2022).

Furthermore, past studies of pyroclastic deposits tend to focus on relatively distal deposits, which typically capture only the most widely-dispersed, hence highest-intensity, eruptive phases (e.g., Singer et al. 2008; Alfano et al. 2011; Bursik et al. 2014; Pistolesi et al. 2015). Lower-intensity phases that are deposited proximally are often discontinuous, difficult to access, and structurally complex, consequently under-represented in reconstructions of eruption dynamics (Hodgetts et al. 2025). Yet, these deposits may record short-lived changes in fragmentation style, degassing efficiency, and conduit processes that are critical for understanding how explosive activity wanes and effusive behavior emerges (e.g. Campbell et al. 2016; Gardner et al. 2019; Trafton and Giachetti 2022). Detailed investigations of near-vent pyroclastic successions therefore offer an opportunity to resolve the explosive-effusive transition at higher temporal resolution.

In this study, we examined several proximal (less than 2 km from the inferred vents) fall deposits from the 877 CE Hrafntinnuhraun eruption of Torfajökull, Iceland, a moderate-intensity rhyolitic eruption, from which past tephra studies had focused on the medial to distal deposits (Larsen 1984). We combine pyroclast component analysis, measurements of dissolved volatile species in pyroclasts, and textural observations, alongside field stratigraphic relationships, to reconstruct the evolution of eruption dynamics during the explosive phase of the eruption. Our investigation indicates that at HRN, the progression from an initially high-intensity stage, via a moderate-intensity, unsteady stage, to final hybrid activity with lava effusion, was marked by several cycles of relatively stronger and weaker pulses. We evaluate these dynamics in the context of the cryptic fragmentation hypothesis, which proposes that silicic lavas and pyroclasts may be assembled in the shallow conduit from previously fragmented ash-rich material (Wadsworth et al. 2020). Finally, we discuss the implications of this interpretation for recognizing hybrid explosive–effusive behavior in the geological record and for assessing hazards associated with silicic eruptions (Zhang et al. 2026).

2 Geological Context

The rhyolitic Hrafntinnuhraun (HRN) eruption occurred in 877 CE (Schmid et al. 2017) within the Torfajökull volcanic system, producing 0.4 km^3 of bulk tephra and 0.18 km^3 of lava (Larsen 1984). As the largest eruption of Torfajökull in historical times (i.e. past c.1150 years) and the second largest in the Holocene (McGarvie 1984; Saemundsson and Larsen 2019), reconstructing the eruptive dynamics of HRN is essential for assessing future silicic eruption hazards associated with the Torfajökull volcanic system.

Larsen (1984) interprets, from the close proximity of the tephras, that the eruption of HRN was simultaneous with the more voluminous (c.3.3 km^3), explosive basaltic eruption of the Veiðivötn (VDV) fissure swarm northeast of HRN, with a combined

fissure length of 42 km. The coupled basaltic and rhyolitic tephra deposits form the stratigraphically-important Landnám ('Settlement') layer (Larsen 1984; Cage et al. 2011) (Fig. 1b) . Paleo-wind direction during the HRN-VDV eruption, northwestwards to westwards, is attributed as the rhyolitic HRN tephra being deposited before the basaltic VDV tephra in localities northwest of HRN (Larsen 1984). The dispersal axes of VDV and HRN tephras are parallel and separated by the distance between their source regions, suggesting that the distally-dispersed explosive phase(s) of HRN was within the eruption window of VDV, estimated to be up to 5 days (Larsen 1984).

The HRN rhyolite is mildly-alkalic with c. 70-72% SiO_2, variably mixed and mingled with a transitional alkali basalt deriving from Torfajökull (McGarvie 1984; McGarvie, David W. 1985; Macdonald et al. 1990). Although there is extensive characterization of the geochemistry of the rhyolitic component of HRN tephras in distal deposits, the lava is the only vent-proximal material that has been the focus of detailed geochemical studies (McGarvie 1984; McGarvie et al. 1990; Macdonald et al. 1990).

The presence of ash-veneered lava surfaces indicates that HRN continued to produce low-intensity ash plumes throughout the entire duration of its lava effusion, likely over timescales of months, displaying similar hybrid activity to Cordón Caulle 2011-2012 (Schipper et al. 2013; Farquharson et al. 2022; Zhang et al. 2026). No related tephra deposits have been documented in medial to distal locations, primarily attributable to the poor preservation potential of the hybrid phase tephra (Zhang et al. 2026).

3 Materials and Methods

3.1 Field observations

Field campaigns to HRN were conducted in 2021, 2022, and 2023, with permits to sample and export its products granted by the Environmental Agency of Iceland and The Icelandic Institute of Natural History.

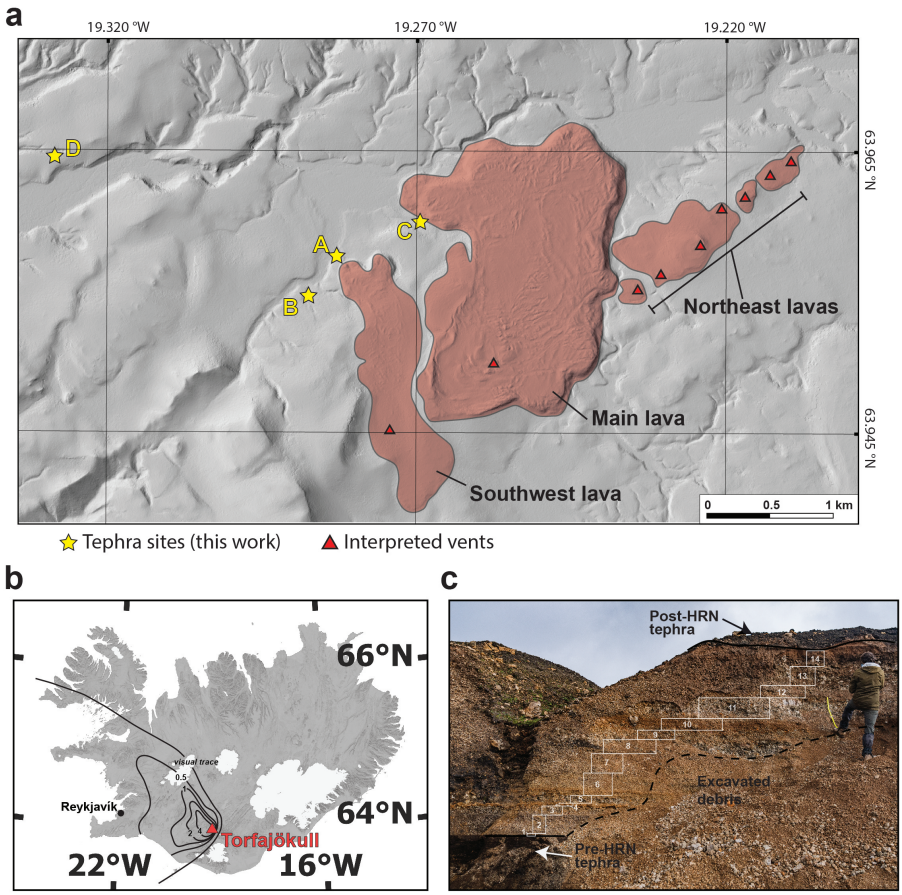


Fig. 1 Overview of the Hrafntinnuhraun (HRN) lavas and tephra distribution. a. Aerial imagery of the HRN area, showing the approximate extent of the lavas, locations of the inferred vents, and proximal tephra deposits. The tephra sites characterized in this study are marked (A-D). The basemap is adapted from a digital elevation model (ÍslandsDEM útgáfa 1.0 by Náttúrufræðistofnun, licensed under CC BY 4.0; accessed via https://gatt.lmi.is). b. An overview map of Iceland showing the location of Torfajökull and the distal isopachs of the HRN eruption, adapted from Larsen (1984). c. A photo of the tephra sequence A (this work), looking southeastwards; Approximate extents of tephra packages (1-14; see main text), as well as pre- and post-HRN horizons, are marked. Note that the debris in the photo has covered surfaces already logged at the time the photo was taken. Geologist in photograph is 1.7m in height.

We inferred vent locations from lava surface structures, initially from aerial photographs, then verified in the field, and assume for simplicity that these correspond to active vents during the explosive phase. Furthermore, we assume the vents associated with the most voluminous lavas ("southwest" and "main" lavas; Fig. 1a) also represent the primary vents during the explosive phase.

Proximal tephra deposits are widespread and locally form layered deposits up to ∼5 m thick. However, the preexisting topography is apparently complex, such that easily accessible, unmodified, and well-preserved deposits are scarce. A 4.5 m thick volcaniclastic deposit located <2 km northwest of the southwest/main vents — "sequence A" — is the most complete proximal tephra sequence that we identified, and thus forms the primary focus of our study. Two additional sequences (B, C) were logged to provide lateral context; A fourth site, D, 2.5 km west-northwest of sequence A, was excavated and selectively sampled. (Fig. 1a)

All four sites are primarily representative of tephra fall deposit – displaying angular clasts/grains, dominantly clast-supported, and volumetrically dominated by juvenile pumice. Where observed, the deposits drape underlying topography and display parallel stratification.

Some outsized clasts within sequences A-C were interpreted to be ballistic juvenile components. It is noted that many of these interpreted volcanic bombs are also commonplace on the ground surface and occur sufficiently close to the assumed vent location (<5 km) to potentially represent part of a proximal bomb field, comparable to those documented in equivalent explosive silicic eruptions (Blong and Blong 1984; Loughlin et al. 2015; Schipper et al. 2021).

We defined packages of pyroclastic materials in sequence A based on apparent grain size and componentry in the field. Each package was described, measured, and sampled in bulk, with ∼500 g of representative material collected for each major package, and ∼100 g collected for the thin (cm-thick), fine-grained packages 1 and 4. Clasts with diameters above 128 mm – i.e. interpreted ballistics – were excluded from the bulk sampling to avoid distorting subsequent analyses of clast componentry.

The uppermost package (14) displays significant lateral variation (over meters) in thickness (∼10-60 cm), with the uppermost few centimeters sometimes mixed with younger, overlying basaltic tephra, likely deposited from later eruptions of Hekla and/or Vatnaöldur (Larsen 1984). This last erupted package may have been partially reworked by wind and/or H_2O to some extent, but consistently caps the underlying

stratigraphy and is apparently rhyolitic, hence we interpret it as a tephra package of HRN.

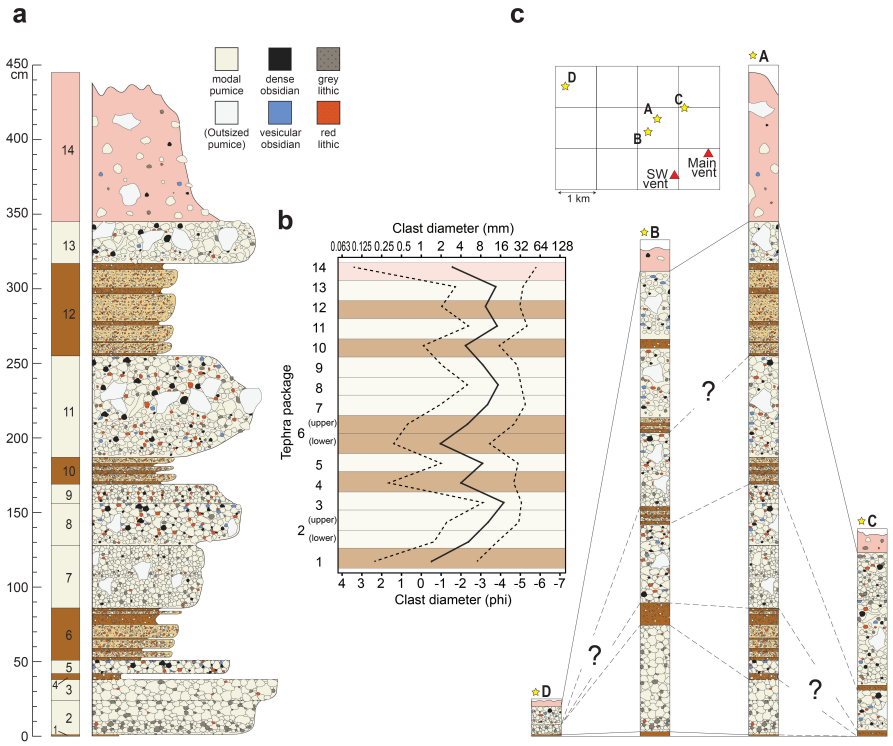


Fig. 2 Graphical logs of the HRN proximal tephra sequences examined in this work. a Graphical log of the main tephra sequence A. b Grain size distribution of packages in sequence A, solid line indicates the mean size, while dashed lines indicate the 10th and 90th percentiles, analyzed via GRADISTAT (Blott and Pye 2001). c Simplified graphical logs of all four sites A-D, with interpreted correlations (dashed lines) between sites. Question marks ("?") denote uncertainty in our correlations. *inset* Simplified locations map of the four tephra sites and two principle vents.

We did not identify any pyroclastic density current (PDC) deposits at any of our tephra sites, but note a possible PDC field, adjacent to and east of the main lava/ south of the northeast lavas, which was not studied in this work. Due to the unknown emplacement directions of possible PDCs, coupled with the focused coverage of our tephra sequences, we do not rule out that additional PDC deposits exist elsewhere in the area, and, by extension, that PDC activity occurred in greater significance during the HRN eruption. Furthermore, as our observations are limited to a total of four

proximal sites, we refrain from re-interpreting the associated plume and medial-distal dispersal of tephra, which is the focus of an ongoing study (Brown, pers. comm.).

3.2 Grain size analysis

Bulk samples of each layer (∼200-500 g) were air dried, then dry-sieved at 1-phi intervals between -7 and 4 phi (128 mm to 63 μm) diameter, which accounts for >90 wt.% of all samples. Each sieved sample was then weighed using an electronic bench-top scale (precision of 0.5 g for components $\gtrsim$10 g, 0.01 g for components $\lesssim$10 g). The data was then analyzed using GRADISTAT (Blott and Pye 2001), for their size distribution characteristics (Folk and Ward 1957).

The <1 mm fractions of packages 3-6 and 11-14 were recombined after sieving, re-homogenized, and analyzed by laser diffractometry using a Beckman Coulter LS-13320 at the Lancaster Environment Centre, Lancaster University, following established methodology (Horwell et al. 2010). Prior to analysis, samples were treated with hydrogen peroxide to remove any potential organic material contaminants, then treated with a 10% sodium hexametaphosphate solution to suppress flocculation. Treated samples were then physically re-homogenized, and from each ∼1 g of material was collected for analysis. H_2O was used as the carrier fluid and dispersant, and a 30 second sonication step was applied immediately prior to each analysis to disaggregate the samples. Three measurement cycles were recorded for each sample, and the average taken. A particle size range of 0.04–2000 μm diameter was measured.

3.3 Clast componentry

Componentry analysis was performed on the bulk tephra samples across the -5 to -1 phi (32 mm to 2 mm) range. This size range was chosen so that a representative mass fraction was available ($\geq$50 wt.% for all samples), and that clast types can be reliably distinguished across the different sizes. Packages 1 and 4 were not analyzed due to the limited amount of available material. Component classifications were designed such

that they can be reliably identified across all phi levels used and are comparable to classifications used in similar studies (Pistolesi et al. 2015).

A subdivision of six clast types is used for this componentry analysis (also shown in Fig. 3 b):

- Modal pumice: high porosity, finely vesicular, angular to sub-rounded, off-white pumices. Vesicles often vary in shapes and sizes within each clast. Phenocrysts are uncommon, often fragmented when present (Fig. 5e), and locally associated with outsized vesicles. Many contain sub-volumes that are visibly tubular, but few comprise the whole clast (i.e. "tube pumice").
- Dense pumice: moderate to low vesicularity, sub-angular to sub-rounded, grey, glassy clasts. Vesicles often strongly deformed, frequently tubular.
- Dense obsidian: Non-vesicular, black, glassy, angular clasts, with characteristic conchoidal fracture. Larger clasts sometimes contain crystals and/or lithic materials.
- Frothy obsidian: clasts with dense obsidian regions as well as distinctly vesicular ("frothy") regions. The frothy regions are typically more coarsely vesicular than pumices.
- Red lithic: non-juvenile, orange to red clasts. The coloration is often patchy and/or limited to sides of the clasts, i.e. likely a surface coating on most such clasts.
- Regular lithic: non-juvenile clasts, most commonly grey in color, of unknown (possibly diverse) compositions. Distinguished from the red lithics by the lack of surficial reddish coloration.

Clasts from each sample were re-homogenized prior to analyses, manually classified with the use of a binocular stereomicroscope, then weighed with electronic bench-top scales (precision of 0.5 g for >8 mm components, 0.01 g for <8 mm components). The weight fractions of components were then combined and normalized to 100% as the total weight fraction componentry for each tephra package.

Two additional, minor clast types were (Fig. 3 b):

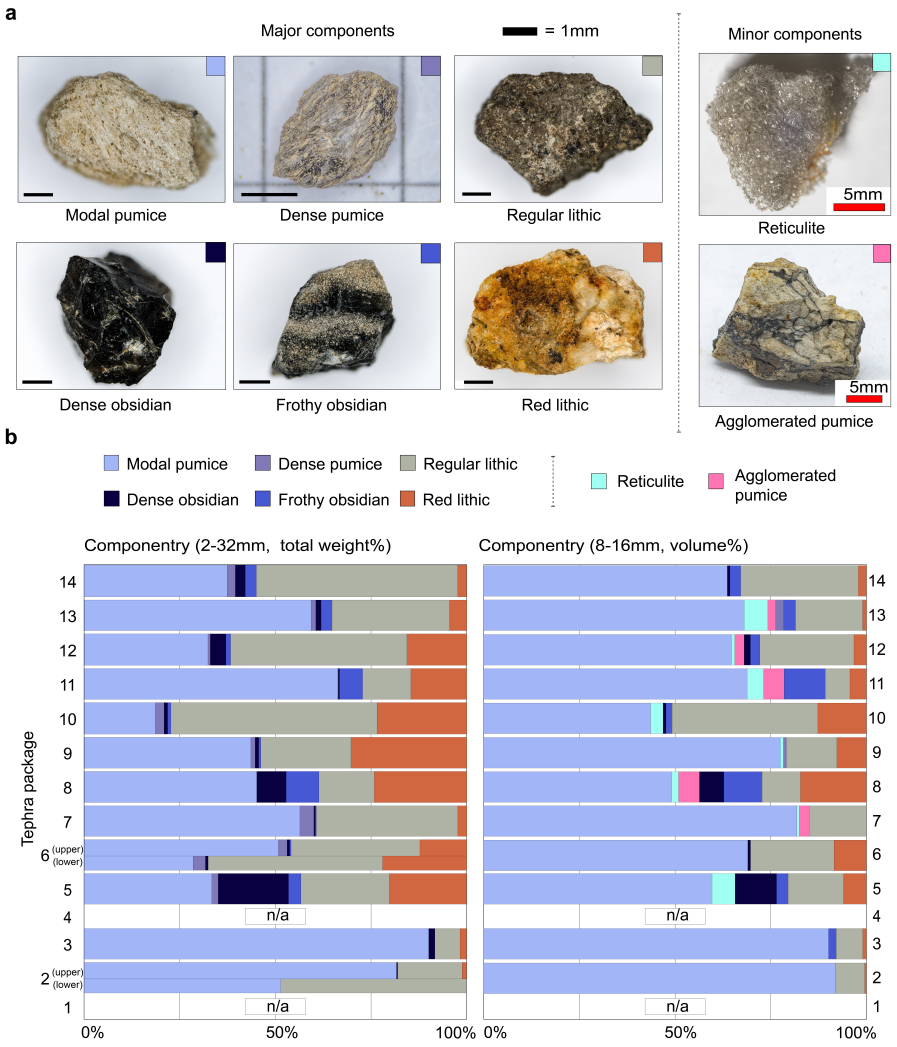


Fig. 3 Grain size and componentry characteristics of sequence A. a. Photographs of representative clasts used in componentry analysis. b Clast componentries of HRN tephra sequence A packages. Note that minor components were only recorded in the 8-16 mm volumetric componentry (see main text).

- Reticulites: very highly porous, coarsely vesicular, foam-like clasts. Vesicles form approximately-equant polyhedral foam. Vesicle walls are mostly intact.
- Agglomerated pumices: pumice clasts containing mm- to cm-scale sub-clasts, with <mm-thick margins in-between, as documented elsewhere (Giachetti et al. 2021). The margins are either pink and ashy, or black and vitreous. Pumiceous sub-clasts

are broadly similar to modal pumices. Some contain obsidian sub-clasts and/or lithic sub-clasts.

These clast types could not be identified consistently across the full size range, yet potentially offer insight into specific dynamics. We recorded numbers (as proxy for volume) of all components – including both minor ones – in approximately 100 g of the bulk material in the 8-16 mm fraction in the 8-16 mm fraction, which corresponds to 100-200 clasts. Packages 1 and 4 were again excluded.

3.4 Geochemistry

We used X-ray Fluorescence (XRF) to characterize modal pumices from layers 2, 5, 8, 11, and 13, in order to examine bulk compositional changes through the course of the eruption. Major and trace element concentrations were analyzed using a Panalytical PW2404 X-ray spectrometer at the School of GeoSciences, University of Edinburgh. Results are reported as oxide weight percentages and normalized to 100 wt.% anhydrous where appropriate. A complete methodology is provided in the Supplementary Information.

3.5 Volatile contents

We performed thermo-gravimetric analysis (TGA) to analyze dissolved volatile contents of a total of 30 obsidian pyroclasts from packages 5-14, as well as modal pumice clasts from packages 2, 5, 6, 8, 11, 12, 13, and 14. Multiple smaller obsidian clasts were combined and analyzed as a single datum for packages 6, 10, and 14 due to a paucity of suitably large obsidian clasts therein. Additionally, we analyzed five variably-vesicular obsidian bombs, collected from the ground surface, and four samples of dense to coarsely-vesicular lavas.

Samples were crushed with a pestle and mortar, sieved to 125-500 μm, rinsed with anhydrous ethanol, then dried for at least 1 hour at 110 °C. The analyses were carried

out using a TA Instruments SDT Q600 system and a Netsch STA449C Jupiter system at the Lancaster Environment Centre, Lancaster University. For each analysis, approximately 40 mg of prepared sample was loaded in an uncovered platinum crucible, heated to 1250 °C at a constant rate of 10 K/minute in a nitrogen atmosphere, following established methodology (Applegarth et al. 2013; Shields et al. 2016). The results were processed to derive the total mass loss (taken to be solely H_2O) from the analyzed material across the temperature windows of 250-550 °C and 550-1250 °C, for secondary and magmatic volatile contents, respectively (Giachetti and Gonnermann 2013; Giachetti et al. 2015).

3.6 Clast porosity

Gas pycnometry analyses were carried out at the Université Clermont Auvergne Laboratoire Magmas et Volcans, in order to ascertain clast porosities, primarily to calibrate the FOAMS analyses. The skeleton volumes of the samples were measured using an AccuPyc II 1340 helium pycnometer, while the bulk volumes were measured with a GeoPyc 1360 pycnometer on parafilm-wrapped samples. Bulk porosities were then calculated using a dense rock equivalent (DRE) of 2.398 g cm^{-3}, calculated from the representative glass composition via DensityX (Iacovino and Till 2019).

3.7 Textural characterization

Transmitted light photomicrographs were collected using a Zeiss Axioscope A1 at the Lancaster Environment Centre, using a Sony ILCE-7RM4 digital camera, using objectives between 2.5x and 50x magnifications. Selected photomicrographs were stitched to form composite images covering the full thin sections for subsequent quantitative analyses.

Scanning-Electron Microscopy (SEM) was used to image various juvenile clasts, fine-grained (<1 mm) materials, and thin sections. Images were collected at the University of Lancaster with a JEOL JSM-7800F SEM. For samples that were to

be quantitatively analyzed for vesicle populations, nested sets of SEM images were acquired, at magnifications 25-1000x.

Image nests, each comprising 12-18 images, were prepared for a representative modal pumice clasts from each of packages 2, 8, and 13. The images were processed in Adobe Photoshop (R) and ImageJ into binary images, then analyzed in FOAMS, following established methodology (Shea et al. 2010), calibrated with clast porosities analyzed via pycnometry (see above).

3.8 X-ray Computed Tomography and flow simulation

X-ray Computed Tomography (XCT) was used to analyze 3D textures of modal pumices. Cylindrical cores (∼8 mm diameter) from representative pumice clasts from packages 2, 8, 13 were analyzed at the Université Clermont Auvergne Laboratoire Magmas et Volcans, using an RX-Solutions EasyTom tomograph, at 2.5-3.5 µm/voxel resolution. An additional pumice clast from package 11 was analyzed at the University of Strathclyde, using a Zeiss 730 XRM, at 3.5 µm/voxel resolution. The reconstructed data were processed and segmented using Thermo Fisher Avizo 3D(R)(version 2024.1). A complete methodology is provided in the Supplementary Information.

We extracted 500×500×500 voxel sub-volumes of XCT scans of modal pumices from packages 2, 8, 11, 13, to perform lattice-Boltzmann flow simulations, in order to investigate the permeabilities and internal flow geometries of the samples (Llewellin 2010a,b). Flow simulations were performed using openLB following established methodology (Schipper et al. 2013; Vasseur et al. 2020).

Packets of fluid mass were propagated through the lattice positions with numerical time t and undergo collisions using a D3Q15 lattice arrangement. We apply a numerical pressure gradient of $\nabla p = 0.01\text{Pa.m}^{-1}$ and an input fluid viscosity of $\mu = 1.8205\times10^{-5}$ Pa s and density of $\rho = 1.2047\text{kg.m}^{-3}$ corresponding to that of air at ambient pressure and temperature conditions. We employ a steady-state criterion such that the average fluid speed across the lattice must not vary by a factor of 10^{-5} twice consecutively over 50 iteration steps (Llewellin 2010a,b). The average fluid velocity at steady state

and in the direction of the applied pressure gradient is given by $\bar{u} = u\phi$ and is used as an input to Darcy's law to compute the permeability. We use conditions for μ and ρ such that the Reynolds and Mach numbers are far lower than unity; for detail, see (Vasseur et al. 2020).

We note that the XCT resolutions used here (2.5-3.5 µm) exceed the lengthscales of textural features, including both vesicles and bubble walls. Given the ubiquity of small bubbles and thin walls within our samples, observed via both optical microscopy and SEM, we deem XCT unsuitable for measuring the vesicle number density, and instead rely solely on the FOAMS-derived values.

4 Results

4.1 Field description

At all four localities (sites A–D), the tephra succession is bounded both below and above by dark, presumably basaltic tephra of unknown provenances (Fig. 1c, 2). All sequences contain a basal, cm-thick, fine-grained package (package 1) likely associated with the initiation/onset of the eruption. The preserved thickness of the tephra sequence is 4.5 m at Site A, 3.3 m at Site B, 1.4 m at Site C, and 0.3 m at Site D. (Fig. 2, see below).

The component proportions of each sub-unit are shown in Fig. 2 and 3. Modal pumice is generally volumetrically dominant. Packages 2-3 contain relatively low lithic material, with negligible red lithics and obsidian clasts. Dense obsidian first appears in substantial quantities in package 5, and is present in subsequent pumice lapilli packages (7-9) but rare to absent in the lithic-rich internally-layered packages (6, 10). From package 11 upwards, obsidian pyroclasts become abundant and present in moderate quantities (5.4 wt.%) in the lithic-rich internally-layered package 12, in contrast to packages 6, 10 (∼1 wt.%). Agglomerated pumices and reticulites occur first in package 5, then occurring in broadly similar patterns with obsidians. Red lithic clasts also first become abundant in in package 5, with their relative abundance – both

as fraction of all clasts, and of non-juvenile clasts – increasing upwards from package 5, reaching a maximum in package 8, before decreasing towards the top of the succession (Fig. 3), differing from the package to-package variability of the obsidian pyroclasts.

4.2 Grain size and component characteristics

The grain size characteristics of tephra sequence A are summarized in Table 1. Overall, the packages can be broadly grouped, by total componentry, into: a) *Light-colored, pumice lapilli packages* (2, 3, 5, 7, 8, 9, 11, and 13): clast-supported, massive, dominated by pumice lapilli, relatively poor in lithic material, containing obsidian pyroclasts above package 4, and frequently large, outsized pumice clasts. Of these, packages 5, 8, 11, and 13 contain relatively more abundant obsidians that are also more texturally diverse. b) *Brown-orange, lithic-rich packages* (packages 6, 10, 12): lithic-rich, parallel inter-layers of slightly coarser, pumice-rich material, and slightly finer, pumice-poor layers. Such inter-layers are 1-5 cm thick and themselves not visibly structured. Considered in bulk, these packages are more lithic-rich than the light-colored pumice lapilli packages. c) *Fine-grained, mud-like packages* (packages 1, 4) : Thin (<5 cm) packages that exhibit extensive particle aggregation. These contain some lapilli-sized clasts but are difficult to characterize due to cohesive clumping and aggregation of clasts within the fine-grained matrix. Of these, package 1 is light grey in color, while package 4 is brown-orange and unusually indurated. d) *Fine-grained, ash-rich package* (package 14). This is a massive deposit supported by a pink ash matrix. In contrast to package 1 and package 4, the ash shows little tendency for aggregation and is instead loosely packed, and contains abundant lapilli-sized clasts.

The analyzed fine-grained fraction of packages 3-6 and 11-14 is summarized in Fig. 4a. The <1 mm fractions of the analyzed packages are approximately bimodal for pumice lapilli packages (3, 5, 11, 13) and package 14, and weakly bimodal to unimodal for inter-layered lithic-rich packages (6, 12). Note that the "peak" at 1 mm common across most samples is probably due to the samples having been sieved to <1 mm. Uniquely, the <1 mm fraction in package 4 is multi-modal and lacks the

Table 1 Clast size characteristics and total weight% componentry of HRN tephra sequence A.

Tephra package	Mean (ϕ)	Sorting	F63 (wt.%)	Mode 1 (µm)	Mode 2 (µm)	Modal pumice	Dense pumice	Frothy obsidian	Dense obsidian	Regular lithic	Red lithic
14	-1.57	V. Poorly Sorted	5.63	12000	93.75	37.4	2.2	2.6	2.9	52.6	2.4
13	-3.76	M. Sorted	0.09	24000	-	59.3	1.2	1.3	2.9	30.7	4.6
12	-3.24	Poorly Sorted	0.01	12000	-	32.3	0.6	4.1	1.2	46.1	15.6
11	-3.83	V. Well Sorted	0.06	24000	-	66.2	0.1	0.3	6.1	12.6	14.6
10	-2.23	Poorly Sorted	0.05	12000	-	18.5	2.3	1.0	0.8	53.9	23.5
9	-3.13	Poorly Sorted	0.03	12000	-	43.6	1.1	0.9	0.6	23.5	30.3
8	-3.88	M. Well Sorted	0.13	24000	-	45.1	0.1	7.6	8.6	14.4	24.2
7	-3.35	Poorly Sorted	0.19	12000	-	56.4	3.7	0.4	0.2	37.0	2.4
6 (upper)	-2.34	V. Poorly Sorted	0.18	24000	3000	50.7	2.3	0.7	0.3	33.7	12.3
6 (lower)	-0.97	Poorly Sorted	0.17	750	3000	28.5	3.2	0.7	0.0	45.6	22.0
5	-3.09	Poorly Sorted	0.15	12000	-	33.3	1.7	18.4	3.3	23.1	20.2
4	-2.00	V. Poorly Sorted	0.73	24000	6000	-	-	-	-	-	-
3	-4.17	V. Well Sorted	0.20	24000	-	90.1	0.0	1.6	0.0	6.6	1.8
2 (upper)	-3.38	Poorly Sorted	0.06	12000	-	81.6	0.1	0.2	0.0	16.9	1.2
2 (lower)	-2.39	Poorly Sorted	0.30	12000	-	51.4	0.0	0.0	0.0	48.6	0.0
1	-0.52	Poorly Sorted	1.38	3000	-	-	-	-	-	-	-

"peak" at ∼1 mm, despite the deposit including clasts >>1 mm in diameter. We interpret that this reflects significant aggregation, and that the disaggregation step during preparation removed all apparent "particles" between ≳0.3 mm, by separating into their constituent, smaller particles. The fine-grained material of package 4 also uniquely display a blocky, "mossy" appearance, contrast to other packages which predominantly comprise pumiceous fragments and vesicle wall shards (Fig. 4b).

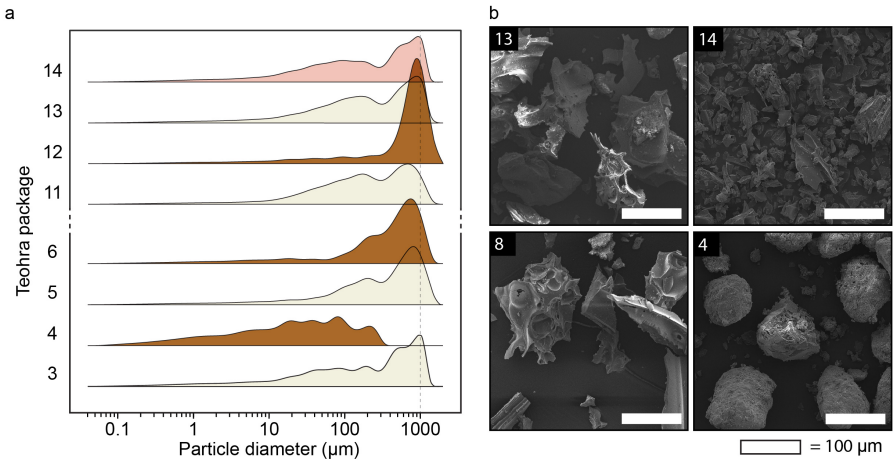


Fig. 4 Characteristics of fine-grained fraction of HRN tephra. a Grain size distributions, for which the distribution area is normalized for comparison and for which the y-axis heights are the volume fractions associated with each particle diameter bin. Note that the samples had been sieved to <1 mm in preparation, indicated by the vertical dashed line. b SEM images of fine-grained materials from packages 4, 8, 13, and 14.

Juvenile clasts frequently show evidence of clastogenesis, including sintering margins, juxtaposed clast types and/or vesicle populations (Fig.5. Crystals are often accompanied by outsized vesicles (Fig.5a), and/or are extension-fractured (Fig.5e), consistent with textures known from Vulcanian products (Giachetti et al. 2010; Miwa and Geshi 2012). Regions within agglomerated clasts are sometimes visibly re-vesiculated (Fig.5d, g). Complete or incipient vesicle wall failure (coalescence) are common (Fig.5c, f, h). Margins between partially-agglomerated clasts sometimes retain voids (Fig.5a), broken/deformed pumiceous material (Fig.5b), and/or pinched,

hair-like structures (Fig.5j), the last consistent with extensional rupture of previously vesicular material (Gillies et al. 2026).

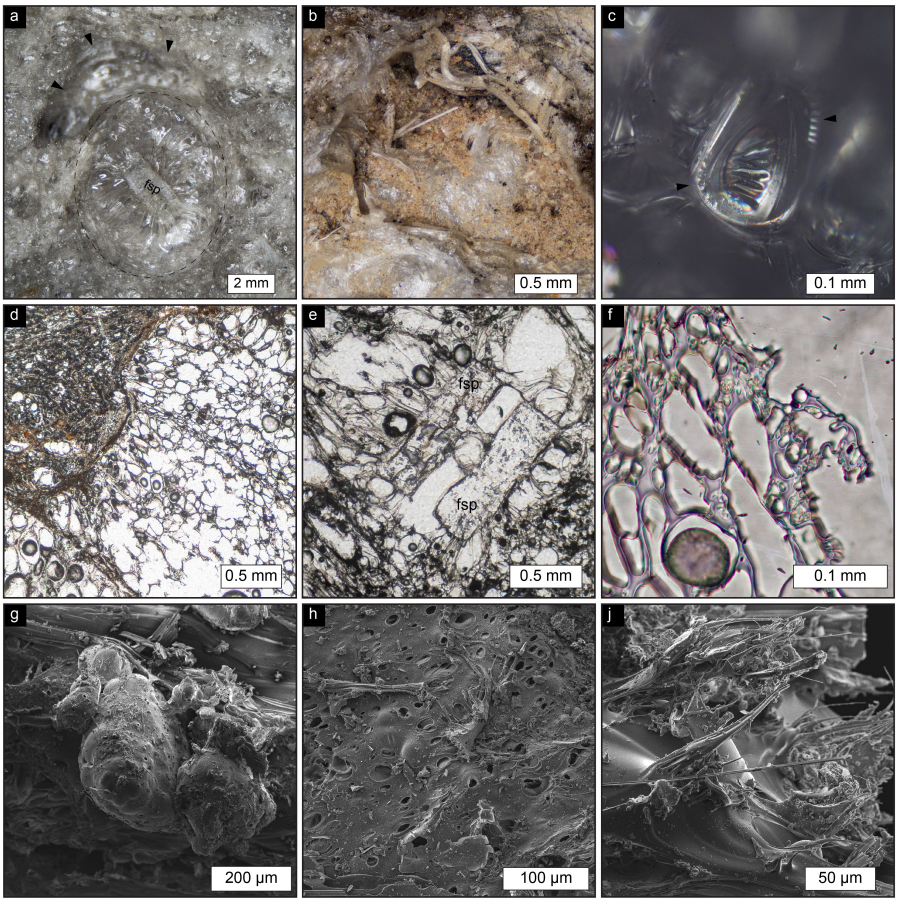


Fig. 5 Reflected-light (a-c), transmitted light (d-f), and SEM images of microscructures of HRN tephra clasts. a Outsized vesicles (dashed circle) surrounding a feldspar (fsp) crystal, within a pumice clasts. Also note the void (black arrowheads), likely a clast margin. b Clast margin of an agglomerated pumice, showing complex deformation history recorded by pumiceous strands. c Wrinkled vesicle wall in pumice clast. Also note the undulatory edges (black arrowheads) of a failed vesicle wall. d Agglomerated pumice clast, showing distinct vesicle populations and denser, moderately-sintered clast margins. e Pull-apart feldspar (fsp) crystal within a pumice clasts. f Strongly-deformed vesicle cluster protruding into a void, within a pumice clasts. g Frothy, achnelith-like clasts sintered to a agglomerated pumice clast. h Smooth surface from melt retraction, topped by glassy, pumiceous fragments. i Hair-like structures, likely formed by ductile pull-apart of a previously-joined clast, on the margin of a agglomerated pumice.

4.3 Geochemistry

The five pumice samples have a mean (normalized, volatile-free) SiO_2 content of 70.44 wt.% (s.d. 0.29 wt.%) and are uniformly rhyolitic (via the total alkali-silicates classification, Fig. 6a), and consistent with previous characterization of HRN eruptive products (McGarvie, David W. 1985).

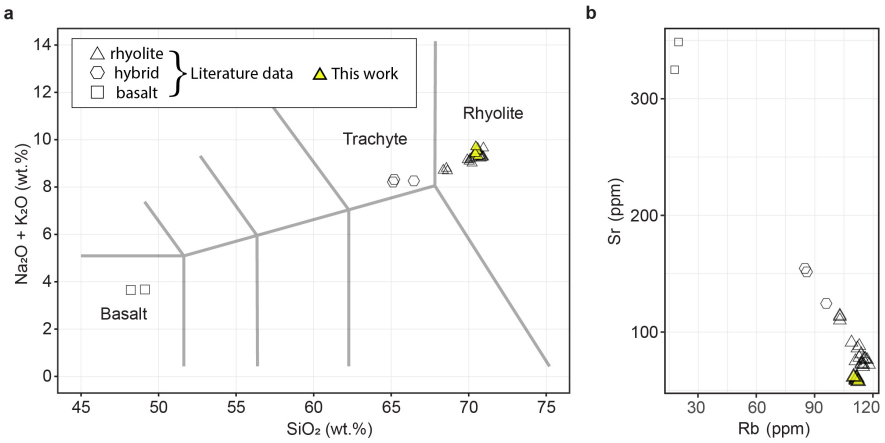


Fig. 6 Major and trace element characteristics of HRN modal pumices, with literature data(McGarvie, David W. 1985; McGarvie et al. 1990) of Torfajökull rhyolites. a Total akali-silica plot. b Sr-Rb plot.

The near-identical compositions of rhyolitic tephra and lava from HRN (McGarvie, David W. 1985) support the genetic interpretation from deposit characteristics that the pyroclastic and lava components are co-eruptive (Wadsworth et al. 2020; Zhang et al. 2026). Additionally, the negligible variation in pumice compositions throughout the tephra sequence suggest that the explosive stage of HRN did not tap a compositionally-stratified reservoir, or was the basaltic melts involved to a significant degree.

Table 2 VND data and median diameter. *Nv – Vesicle number densities per volume. ** Nv_{corr} – Vesicle number densities per volume, corrected for vesicularity.

Tephra package	Porosity (vol.%)	Nv (m^{-3}) *	Nv_{corr} (m^{-3}) **	Median diameter (μm)
13	82.6	1.06×10^{16}	6.11×10^{16}	52.13
8	86.0	2.53×10^{16}	1.81×10^{17}	88.19
2	80.6	3.00×10^{15}	1.55×10^{16}	66.92

4.4 Vesicle characteristics

The analyzed vesicle number density (VND) are summarized in Table 2. All three VNDs are high, between 1.55×10^{15} and 1.81×10^{17} m^{-3}, with the highest value occurring in the package 8 sample. Smallest bubble diameter characterized for all three samples are within the 0.47-0.59 μm bin. Vesicle size distribution (VSD) plots (7) display prominent peaks at ∼14.7–18.5 μm, ∼46.5 μm, and ∼233.1–293.5 μm in all samples, and additional peaks at larger bubble sizes in pumices samples of packages 8 and 13.

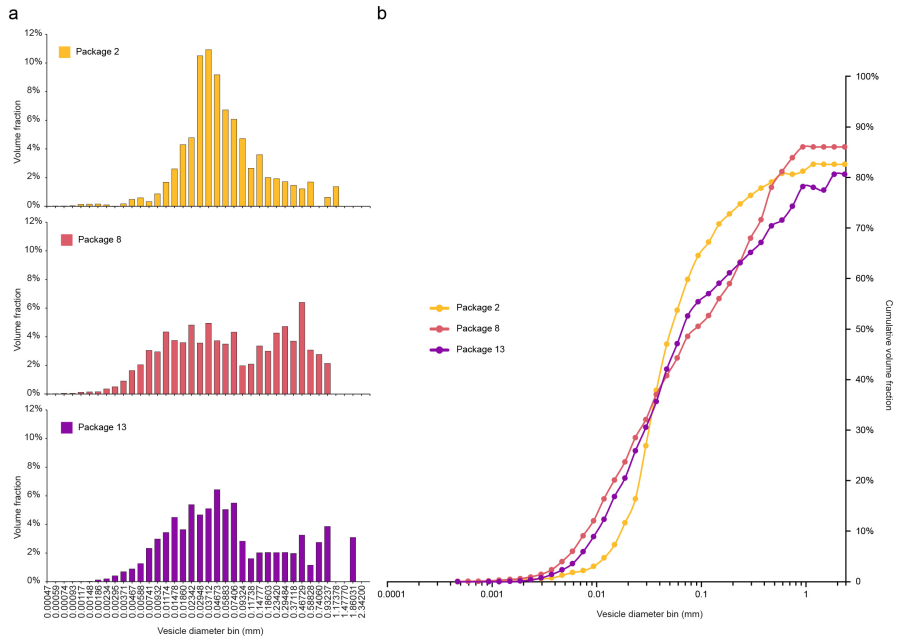


Fig. 7 FOAMS plots. a Volume fractions by diameter bins. b Cumulative volume fraction against vesicle diameter.

4.5 Porosity and permeability

The openLB-derived permeabilities are 3.35-6.05×10^{-12}m^2, 7.27-11.9×10^{-12}m^2, 7.57-34.2×10^{-12}m^2, 3.37-27.7×10^{-12}m^2, respectively, for pumice samples of packages 2, 8, 11, 13, broadly consistent with reported permeabilities from other silicic eruptions (Colombier et al. 2017). All four samples analyzed have similar permeabilities and anisotropy, slightly increasing in the later packages. Flow simulations derived from openLB are visualized, alongside corresponding transmitted light photomicrographs and rendered XCT volumes, in Fig. 8.

4.6 Dissolved volatile contents

TGA data of a total of 60 samples are summarized in Fig. 9. Obsidian pyroclasts within package 5 (i.e. their main onset) contain the highest magmatic H_2O contents, at ∼1.5 wt.%, sharply decreasing to ∼1.0 wt.% in package 6, then maintained an overall slow decreasing trend up the sequence to ∼0.8 wt.% in package 14. Obsidian bombs from the deposit surface are, on average, lower at ∼0.6 wt.% but show a wide range, overlapping the range of volatile contents recorded in the upper packages (i.e. 11-14). Volatile contents of the lava samples are more tightly clustered around 0.3 wt.%, overlapping with the range of obsidian bombs and broadly consistent with other studies of subaerial lavas (Shields et al. 2016; Wadsworth et al. 2020). In contrast, the volatile contents of modal pumice clasts overall show a weak increasing trend upwards, from a mean 0.56 wt.% in package 2 up to a mean 0.73 wt.% in package 13. (Fig. 9a).

The speciation of secondary versus magmatic H_2O (Denton et al. 2012; Giachetti et al. 2015; Shields et al. 2016) shows two distinct clusters between obsidian pyroclasts (variable magmatic H_2O, consistent low secondary H_2O) and pumices (consistent low magmatic H_2O, variable secondary H_2O), summarized in Fig. 9b. Frothy obsidians, despite having comparable porosities to co-located pumices, instead follow the cluster of dense obsidians, which suggests that they are co-genetic and frothed at low pressure

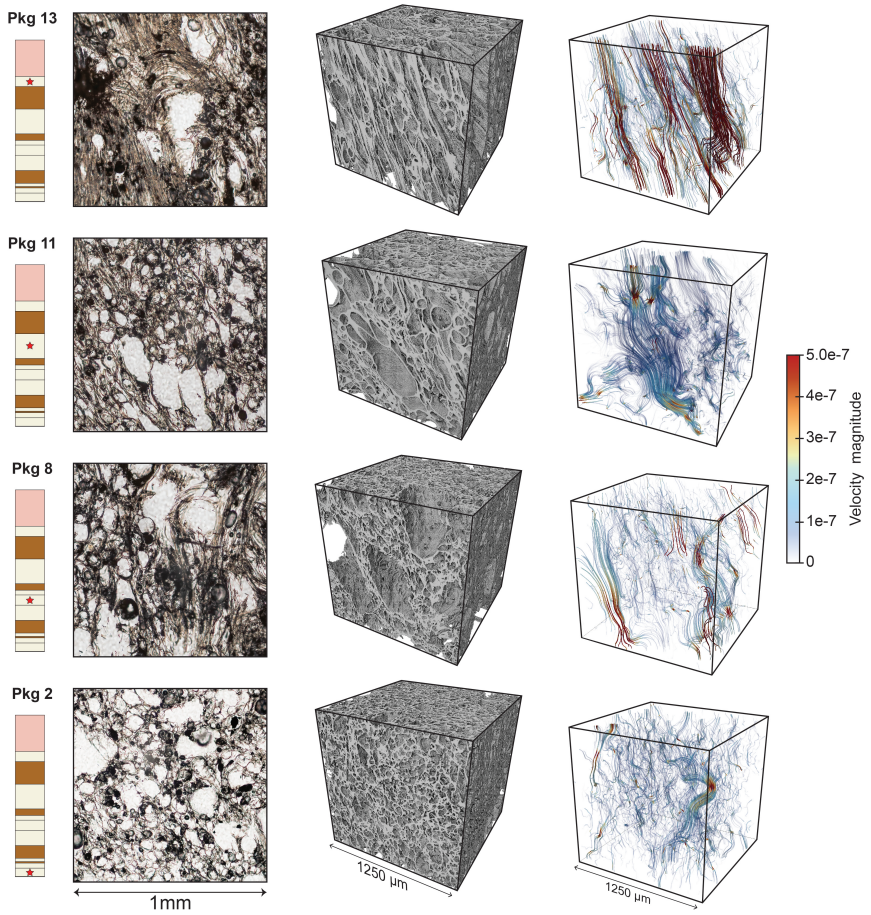


Fig. 8 Characteristics of pumices. Left to right, stratigraphic context of the samples, corresponding transmitted-light photomicrograph of thin sections, rendered binarized XCT data of the sub-volumes used for flow simulations, and visualized streamlines. XCT visualizations were made in Thermo-Fisher Avizo(R), where, the solid phase (glass and any crystals) is rendered in grey, while the pore spaces are not rendered (i.e. are invisible). Streamline visualizations were prepared using ParaView, showing the fluid flow velocities from the OpenLB simulations, which underpin the permeability values.

with no major dissolved H_2O loss. The surficial obsidian bombs and lavas, which cover a range of porosities, similarly follow the obsidian pyroclasts cluster.

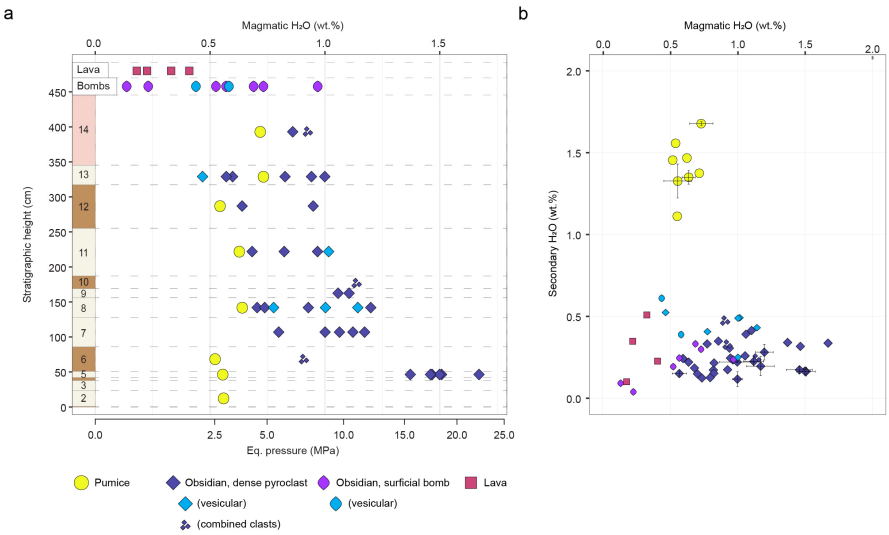


Fig. 9 Volatiles content data. a Magmatic volatile contents of analyzed clasts (n=60) through the main tephra sequence. b Secondary H_2O versus magmatic H_2O of analyzed clasts. Error bars (where present) indicate the ranges of values attained from multiple analyses of the same sample.

5 Discussion

5.1 Vesicle populations and eruption intensity

The vesicle size distribution plots can be used to reconstruct processes such as nucleation, coalescence, and growth (Shea et al. 2010; Alfano et al. 2012). The presence of multiple peaks at 14.7–18.5 µm, 46.5 µm, and 233.1–293.5 µm (Fig. 7) can be interpreted as three distinct phases of nucleation and growth, across all three samples. The smallest vesicle population indicates continuous or accelerating nucleation until fragmentation (Houghton et al. 2010). The package 2 sample displayed minimal coalescence signature, unlike packages 8 and 13, which exhibit pronounced signature of coalescence (Shea et al. 2010). This is consistent with increased scope for degassing and textural maturation later in the eruption, as the intensity waned and conduit constricted (Wadsworth et al. 2022).

Conventionally, VNDs are interpreted based on experimental decompression rate-meters, where high VNDs are the result of high decompression rates, which are then linked to higher-intensity eruption dynamics (Toramaru 2006; Houghton et al. 2010;

Hajimirza et al. 2019). The relationship between VND and decompression rate is complicated by the occurrence of heterogeneous nucleation (Shea 2017), where nanolite populations present prior to vesiculation (Cáceres et al. 2020; McCartney et al. 2025) promote bubble nucleation.

The three analyzed pumices from packages 2, 8, and 13 exhibit high VNDs ($\sim 10^{17}$ m^{-3}; 2), broadly comparable with the higher end of reported VNDs of Plinian rhyolitic eruptions (Gardner et al. 2023). Assuming that for HRN the pumice VNDs are correlated to eruption intensity, then its climactic phase was that recorded by package 8, i.e. approximately the middle of the tephra sequence. This differs to the eruptions of Chaitén 2008 and Cordón Caulle 2011-2012, the climactic phase of both occurring at the onset of the entire eruption period (Pallister et al. 2013; Pistolesi et al. 2015). Nevertheless, we note that such a sequence would not be unprecedented, with the climactic phases of $\sim 1/3$ of eruptions occurring in the latter half of their full durations (Cassidy et al. 2018).

Workers have cautioned that the relationship between mass eruption rates, decompression rates, and VND is not straightforward in rhyolitic tephra (Alfano et al. 2012), partly due to disequilibrium favored by high melt viscosity (Rust and Cashman 2011). Populations of micro/nano-lites, which evolve through the course of an eruption, also contribute to greater VNDs not associated with the eruption intensity (Shea 2017). While our optical microscopy and SEM imaging did not reveal noticeable differences in microlite populations through the sequence (and could not resolve potential nanolites), microlites are systematically underrepresented in thin sections due to very low sectioning probabilities (Shea 2017).

Finally, we caution that only three pumice clasts were analyzed in this study, all selected from pumice lapilli packages. Further work should expand the sample set in order to improve representativeness, and also analyze pumice clasts from lithic-rich packages to more thoroughly characterize temporal variations in the vesicle population of HRN pyroclasts.

5.2 Volatile contents and ascent-degassing pathways

Measurements of dissolved magmatic H_2O using TGA analysis (Fig. 9) provide information on temporal patterns of degassing of a variety of clast types, principally dense obsidian and pumice. The relationship between primary and secondary H_2O contents is consistent with past studies (e.g. Giachetti and Gonnermann 2013; Giachetti et al. 2015; Shields et al. 2016) and indicates greater hydration by secondary H_2O in more vesicular clasts, due to their higher specific surface area. Vesicular obsidian clasts in units 8, 11, and 13 have broadly similar H_2O concentrations to their dense counterparts. Lava samples have significantly lower concentrations, as expected, due to degassing towards atmospheric pressure (Shields et al. 2016). By contrast, pumice H_2O concentrations gradually increase from ~0.5 wt.% towards ~0.7 wt.% between packages 2 and 14. We now interpret these values and their significance by considering two contrasting pressure-depth models.

In order to approximate the extraction depths of pyroclasts from their volatile concentrations, we have used the open conduit scenario (Wadsworth et al. 2022) that is relevant for obsidian pyroclast formation at conduit walls, and applied the established conduit model of Degruyter et al. (2012) to calculate a range of conduit depth-pressure relationships. Starting parameters used are a VND value of 10^{17} m^{-3} — i.e. the approximate mean of the three analyzed pumice in this work, an initial H_2O content of either 2 wt.% as representative of Icelandic rhyolites (Saubin et al. 2021), or 5 wt.% as the highest melt inclusion H_2O recorded from Torfajökull rhyolites (Owen et al. 2013b), a typical rhyolitic magmatic temperature of 850 °C, and typical rhyolitic melt density of 2400 kg m^{-3} (also see above), and conduit radii of 10 m, 20 m and 50 m. We use an experimentally-derived pressure-H_2O solubility relationship (Liu et al. 2005) to calculate the equilibrium H_2O contents over the pressure ranges calculated using the Degruyter et al. (2012) model. The strong non-linearity of the pressure-depth relationships involves an abrupt pressure decrease at the depth of modeled fragmentation. A summary of these findings are given in Table 3.

Table 3 Magmatic H_2O contents of HRN obsidian clasts, corresponding equilibrium pressure, and depths in conduit. Depths are calculated as (i) open conduit via Degruyter et al. (2012), with initial H_2O of 2%; (ii) open conduit via Degruyter et al. (2012), with initial H_2O of 5%; (iii) Magmastatic, with column density of 2400 kg m^{-3}.

Group	Magmatic H_2O (wt.%)	Equilibrium P (MPa)	D_{open}, H_2O_{ini}=2% (km)	D_{open}, H_2O_{ini}=5% (km)	$D_{magmastatic}$ (km)
Lavas	0.18-0.41	0.31-1.56	0.07-0.84	0.005-0.05	0.01-0.07
Bombs	0.14-0.97	0.18-8.13	0.008-1.3	0.001-3.9	0.008-0.36
pkg 11-13	0.57-1.02	2.97-8.90	1.2-1.3	1.2-3.9	0.13-0.39
pkg 7-9	0.70-1.20	4.45-12.13	1.3	3.9	0.19-0.54
pkg 5	1.37-1.67	15.54-22.31	1.4-1.5	4.2-5.6	0.67-0.99

These inferred quarrying depths are broadly similar but on the lower side of the depth range inferred from previous studies that have applied linear magmastatic pressure (closed conduit) regimes: for Chaitén bombs within pyroclastic density current deposits and associated with transient Vulcanian explosive events (Castro et al. 2014), and fragmentation depths inferred from lithic clasts at Mt. Meager (Campbell et al. 2016). Conduit depths are also similar to inferred quenching depths of H_2O-rich Torfajökull obsidians (Owen et al. 2012, 2013b) that were emplaced sub-glacially and quenched beneath ice (0.3-0.7 wt.% at Bláhnúkur, and ∼0.5-0.7 wt.% at Dalakvísl), at elevated confining pressures.

Notably, package 5 obsidians consistently reflect equilibrium pressures above the fragmentation pressures in the open conduit models (Fig. 3b). This may be due to re-equilibration to a higher pressure due to conduit obstruction (and subsequent re-pressurization), discussed below.

Applying a closed-conduit linear pressure model to our data, to permit direct comparison with earlier case studies (Saubin et al. 2016; Tuffen et al. 2008), then for a mean column density of 2400 kg m^{-3} the dissolved H_2O concentration of juvenile obsidians translates to depths of ∼820 m for the package 5 obsidians, while the package 7-13 sequence represents a moderate shallowing from ∼400m to ∼210m, the surficial bombs represent depths of 7-350m, and the lavas represent depths of 14-68m (Fig. 10a). Once again, the package 7-13 obsidians and surficial bombs yield similar depths to those inferred for Chaitén bombs (Saubin et al. 2016), and quenching

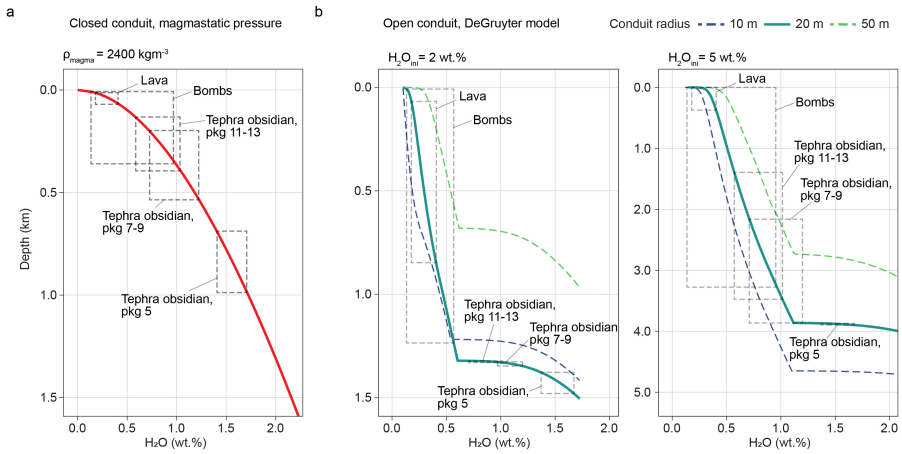


Fig. 10 Magmatic volatile contents of HRN juveniles and equilibrium pressures. a Magmastatic pressure model. b Open-conduit model, calculated using Degruyter et al. (2012). Boxes with dashed borders indicate the ranges of magmatic H_2O and corresponding depths of the groups, using the 20 m radius conduit models for both open conduit plots.

depths beneath ice/melt H_2O elsewhere at Torfajökull. (Tuffen et al. 2008; Owen et al. 2013b).

The significance of dissolved H_2O concentrations in pumiceous silicic clasts has received less attention than corresponding values in dense obsidian pyroclasts (Owen et al. 2013a; Castro et al. 2014; Saubin et al. 2016), as complex vesiculation and degassing histories hinder pressure reconstruction, and primary magmatic volatiles in pumices are readily overprinted by secondary hydration due to their high specific surface area (Giachetti and Gonnermann 2013; Giachetti et al. 2015). We recognise that the vesicle wall width exerts a strong control on the H_2O loss patterns from rhyolitic pumices (Giachetti et al. 2015), and quantification of these widths, required for precise primary H_2O quantification, is beyond the scope of this current study. Nonetheless, our approximation from >550 °C weight loss does permit useful inter-package comparison and an approximate comparison of H_2O in pumiceous and dense pyroclasts.

The inferred quenching pressure for pumiceous pyroclasts is markedly lower than the dense obsidian when their lower H_2O contents are considered, and a similar discrepancy in sub-glacially erupted Torfajökull glasses (Tuffen et al. 2008; Owen et al.

2012) was related to the high porosity of samples, with closed-system expansion of initially dense magma inferred from the apparent lack of welding and sintering textures. The pumices of the HRN sequence show a very weak upwards increasing trend in dissolved H_2O, opposite to that of the obsidians. Here, the lower pumice H_2O does not indicate closed-system degassing of dense obsidian, as was inferred for variably pumiceous zones of rhyolitic sheets at Torfajökull (Owen et al. 2013b). Instead, we infer a different degassing pathway for the dense and pumiceous material. The dense obsidian derives from fragmentation of sintered magma at the conduit walls, with the depth of quarrying gradually decreasing during the eruption. In contrast, the pumice clasts derive from the conduit center and the depth of fragmentation gradually increased as the effective conduit width narrowed, and likely experienced non-equilibrium degassing during vesiculation (Birnbaum et al. 2026).

5.3 Possibility of a lull/pause in activity

No signs of extended pauses during the explosive component of HRN had been previously identified from its deposits (Larsen 1984). Nevertheless, days to weeks-long quiescence between otherwise sustained explosive activity had been previously described from the 1960 eruption of Cordón Caulle (Lara et al. 2004). During the 1912 eruption of Novarupta, USA, two abrupt, hours-long gaps were inferred/(partially-)witnessed between episodes of explosivity, prior to emplacement of its lava dome/plug (Adams et al. 2006). Similarly, a short pause in explosivity was also interpreted in two separate (sub-)Plinian phases of the 640 CE eruption of Newberry, USA, recorded as a series of ash layers (Rust and Cashman 2007; Trafton and Giachetti 2022).

We interpret the fine-grained package 4 in the main sequence as representing deposition following a brief lull or pause in explosive surface activity. The abrupt transition from packages 2-3 to 4, with no significant change in clast size or componentry, suggests that this interruption was primarily non-magmatic in origin. We propose that the pause resulted from the collapse of wall rock in the upper conduit, temporarily disrupting explosive activity before deposition resumed (Macedonio et al. 1994).

It can be noted that a similar (hours-long) pause occurred between episodes II and III of the 1912 eruption of Novarupta, USA (Adams et al. 2006). Package 4 material can then be best understood as the deposit of the initiating blast preceding resumed activity represented by package 5 onwards.

We highlight that the first significant occurrence of obsidian pyroclasts, in the overlying package 5, contains substantially more volatile-rich obsidian (∼1.5 wt.%) than obsidians in subsequent packages. Assuming that package 5 obsidians had reached equilibrium, this volatile content corresponds to a confining pressure of ∼18 MPa, consistent with modeled overpressures required to drive tuffisite opening around ascending rhyolitic magma (16-29 MPa, Unwin et al. (2021)), and is approximately equivalent to the gravitational pressure of ∼800 m of overlying rock. We interpret these high magmatic H_2O values as evidence for a pause associated with a top-down blockage (Schipper et al. 2021; Wadsworth et al. 2022), potentially resulting from conduit collapse following package 3. This blockage may have allowed the conduit to re-pressurize,causing juvenile obsidians within the conduit to re-equilibrate towards higher pressures. These conditions were then apparently not repeated during the remainder of the eruption.

Red lithics also become abundant in package 5, having only been present in trace amounts in earlier packages. In the context of a top-down blockage, we propose two possible explanations: (a) the red lithics represent pre-existing, altered country rock that was spatially adjacent to the initial HRN conduit but not initially excavated during the early stages of the eruption. Their subsequent appearance in package 5 may therefore reflect a change in the depth of quarrying (Campbell et al. 2016) and/or the lateral propagation of the fissure, bringing this material into the zone of excavation; (b) Alternatively, blockage inducing conditions may have promoted degassing into the conduit margins and the blockage breccia, facilitating rapid alteration of the country rock (Hoult et al. 2025). This process could have generated an in situ stock of red lithics available to be excavated by subsequent explosivity after activity resumed. Given the apparent ubiquity of red, hydrothermally-altered older formations exposed in stream

valleys close to the eruptive fissure, and the evidence for multiple active vents in the HRN eruption, we tentatively favor model (a). However, distinguishing between these interpretations will require more detailed characterization of the alteration assemblage and comparison with the composition and textures of local country rock lithologies.

Finally, the fine-grained, matrix- and lithic-rich componentry of package 4, together with the distinctly "mossy" appearance (Zimanowski et al. 2015) of its ash particles (Fig. 4b; Cas et al. (2024)) may additionally indicate interactions with external subsurface water. Such volcano-water interaction could have promoted wall rock excavation (White and Valentine 2016) and enhanced fragmentation to a finer grain sizes (Walker 1973). This interpretation is further supported by a high degree of clumping between ash particles, which is favored during moist plume conditions (Costa et al. 2010). Nevertheless, our observations do not allow us to determine the extent to which external water influenced the eruptive dynamics of package 4, or whether its involvement is consistent with the lull or pause in explosive activity proposed above.

5.4 A proximal tephra record of the hybrid phase?

The continuity of obsidian H_2O contents from packages 11-14 onward to the surficial obsidian bombs suggest that these packages mark the transition from explosive to hybrid behavior. The distinctly high ash content of package 14 (Table. 1) can be interpreted as evidence for lower-intensity and fracture-filtered output. Simultaneously, its multi-modal size distribution (Fig. 4) is consistent with increased secondary fragmentation (Trafton and Giachetti 2022). Hence, both observations may indicate that package 14 record the final hybrid activity.

Nevertheless, no comparable proximal tephra sequence from an observed hybrid silicic eruption currently provides a verified record of the onset of hybrid activity, against which to test our interpretation. We therefore consider these interpretations tentative and propose that they provide a framework for future investigation of proximal silicic tephra sequences, particularly those preserving transitions into hybrid eruptive behavior.

5.5 A schematic of the HRN explosive eruption

We present a unified schematic of HRN's explosive eruption, focusing on its conduit dynamics, that best accounts for our interpretations of the proximal tephras, as follows (summarized in Fig. 11): 1. Onset and initial explosive phase The eruption may have begun with hydromagmatic or phreatomagmatic explosion(s) – as recorded by the fine-grained basal package 1 – then rapidly intensified, represented by the coarse pumice lapilli packages 2-3 (Fig. 11a). Conduit wall erosion was rapid and out-paced any syn-eruptive alteration to the country rock or generation of conduit-wall lining via sintering.

2. Lull/pause in activity The first explosive phase of HRN apparently collapsed rapidly into a lull/pause (Fig. 11b). We propose a conduit blockage by country rock as the cause for HRN's lull, similar to proposed events at Novarupta (Adams et al. 2006). The conduit re-pressurized up to ∼18 MPa, with low (if any) surface activity occurring during this likely hours-long window.

3. Strong pulsatory phase The eruption resumed with Vulcanian activity, initiating, following the lull/pause, with a possible hydromagmatic blast (Fig. 11c). The first pulse (package 5) excavated sintered lining on the conduit wall, ejecting high-H_2O obsidian pyroclasts, and either (a) widened/shifted the conduit to excavate previously un-tapped red lithics from country rock, or (b) excavated the recently-formed red lithics along conduit margins and the breccia plug.

A quasi-cyclic sequence of moderate-low intensity pulses (packages 6, 10) and obsidian-excavating, higher-intensity Vulcanian pulses (packages 5, 7-9) occurred. The near-absence of obsidians in the former represents either (i) depletion of sintered lining during the preceding, higher-intensity pulse, and/or (ii) shifting excavation depths such that the lining was not actively excavated. The pulse corresponding to packages 7-9 possibly reached the highest intensity during the entire eruption, evidenced by its pumice VND.

4. Weak pulsatory to transitional phase From package 11 onward, the explosive pulses had gradually weakened, such that either the formation of the sintering lining had begun to outpace its depletion during higher-intensity pulses (following model i) and/or the obsidian lining had become so vertically extensive that it was always excavated (following model ii). Red lithics decreased relative to regular grey lithics, indicating either a shift in the depth or position of excavation (following model a), or depletion of syn-eruptive altered country rock (following model b).

The eruption eventually transitioned into hybrid activity (Fig. 11d), with low-intensity lava-synchronous ash venting (Zhang et al. 2026). Package 14 may represent the proximal tephra record of this activity and thus would be the first deposit identified of its kind in the geological record attributed to this recently recorded process.

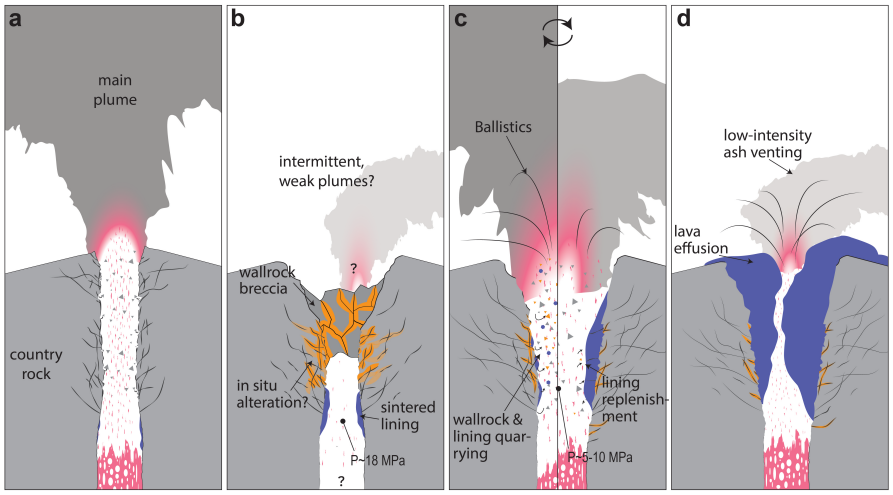


Fig. 11 Schematic illustration of our interpretation of the HRN explosive eruption. a the first explosive phase, corresponding to packages 2-3. b A lull or pause in explosive activity, caused by collapsed conduit wall, allowing re-pressurization of the conduit. Possible in situ alteration of wallrock is illustrated. c Semi-cyclic, pulsatory phases, comprising stronger, lapilli-depositing pulses, and weaker, unstable phases. The sintering conduit lining may be depleted during the stronger phases and replenished during weaker phases. d Transitional to hybrid phase, when the clastogenic lining develops up to and exits the vent as lava. Low-intensity ash venting, indicating sustained fragmentation at depth, continues throughout HRN's lava effusion.

6 Conclusions

We present a detailed characterization of the proximal silicic tephra sequence produced by the 877 CE eruption of Hrafntinnuhraun, Torfajökull, Iceland. The sequence records repeated fluctuations in eruptive intensity, including at least four higher-intensity explosive pulses, separated by lower-intensity activity and/or brief pauses. The alternation of pumice-rich and lithic-rich deposits, combined with the estimated timescale of the eruption (∼5 days), indicates that these changes occurred on timescales of hours. The characteristics of package 4 further suggest that external water may have influenced fragmentation and eruption dynamics, although its role relative to the inferred pause in explosive activity is unclear.

Volatile concentrations in obsidian pyroclasts provide evidence for changes in conduit pressure and excavation depth during the eruption. The unusually high volatile contents of obsidians in package 5 are consistent with storage and re-equilibration at elevated pressure following temporary conduit closure, potentially associated with a top-down blockage from conduit collapse. Subsequent decreases in obsidian volatile contents are consistent with progressive shoaling of the effective excavation depth, culminating in lava effusion. Pyroclast microtextures are consistent with a clastogenic origin of dense obsidian pyroclasts, aggregation of pumices, and sintering-driven assemblage of lava.

Together, the stratigraphic, componentry, volatile, and textural characteristics of the Hrafntinnuhraun sequence indicate that the transition from explosive activity to effusion was accompanied by repeated changes in conduit pressure, excavation depth, and fragmentation conditions. The deposits therefore provide a record of short-timescale variability in silicic eruptive behavior. Comparison with medial and distal deposits will allow these proximal changes to be evaluated in the context of plume development, dispersal, and the potential contribution of multiple vents.

Supplementary information. This manuscript is accompanied by a Supplementary Information document, containing: (a) Complete XRF methodology, (b) FOAMS

resolutions and image nests, and (c) Complete XCT methodology. It is also accompanied by the supplementary datasets: (a) total grain size data and GRADISTAT analysis results, (b) H_2O contents data (via TGA analyses), (c) Major and trace elements geochemistry (via XRF analyses), combined as a .xlsx spreadsheet.

Acknowledgments. J. Z. thanks Bo Pan for support with sample preparation, Sara Baldock for assistance with SEM imaging and analyses, Vassil Karloukovski for assistance with laser diffractometry and TGA analyses, Gus Calder for his assistance with XRF analysis, and Daniel McMahon and Natasha Spangrud for their assistance in the field. We thank the Environmental Agency of Iceland and the Icelandic Institute of Natural History for sampling and export permissions, and the Fjallabak rangers for their support in the field. We thank Margherita Polacci, Thomas Jones, Michael James for feedback and discussion.

7 Declarations

7.1 Funding

J.Z. was financially supported by the Henry Emeleus fieldwork award by the Volcanic and Magmatic Studies Group. A.G.E.H. was supported by a University of Edinburgh Earth and Planetary Sciences small grant. M.G. was supported by the InVolc program of Université Clermont Auvergne. H.T. and F.B.W. acknowledge support from NERC grant NE/X015440/1. C.J. is supported by the SNSF grant #P230579 . This research was supported by the IM3AGES Facility through EPSRC grant EP/Z531133/1 and the NXCT under UKRI3067.

7.2 Competing interests

The authors have no competing interests to declare that are relevant to the content of this article.

7.3 Ethics and Consent to Participate

Not applicable.

7.4 Availability of data and material

All data generated in this study are included as Supplementary Information/Datasets, and available via Zenodo (https://doi.org/10.5281/zenodo.22707843). XCT data are available upon request.

7.5 Author contribution

J.Z. – Conceptualization, Methodology, Formal analysis, Investigation; Writing - Original Draft, Review & Editing, Visualization. A.G.E.H. – Methodology, Investigation; Supervision; Writing - Original Draft, Review & Editing. M.G. – Formal analysis, Investigation. H.T. – Conceptualization, Investigation, Supervision; Writing - Original Draft, Review & Editing. D.M. – Conceptualization, Investigation, Resources, Supervision; Writing - Original Draft, Review & Editing. F.B.W. – Conceptualization; Writing -Review & Editing. J.V. – Investigation. C. J. – Investigation. K.J.D. – Resources. S.F. – Investigation. L.G. – Resources, Supervision; Writing - Review & Editing. A.H. – Resources, Supervision. D.F.S. – Project administration.

References

Adams NK, Houghton BF, Hildreth W (2006) Abrupt transitions during sustained explosive eruptions: examples from the 1912 eruption of Novarupta, Alaska. Bulletin of Volcanology 69(2):189–206. https://doi.org/10.1007/s00445-006-0067-4, URL http://link.springer.com/10.1007/s00445-006-0067-4

Alfano F, Bonadonna C, Volentik ACM, et al (2011) Tephra stratigraphy and eruptive volume of the May, 2008, Chaitén eruption, Chile. Bulletin of Volcanology 73(5):613–630. https://doi.org/10.1007/s00445-010-0428-x, URL http://link.springer.com/10.1007/s00445-010-0428-x

Alfano F, Bonadonna C, Gurioli L (2012) Insights into eruption dynamics from textural analysis: the case of the May, 2008, Chaitén eruption. Bulletin of Volcanology 74(9):2095–2108. https://doi.org/10.1007/s00445-012-0648-3, URL http://link.springer.com/10.1007/s00445-012-0648-3

Applegarth L, Tuffen H, James M, et al (2013) Degassing-driven crystallisation in basalts. Earth-Science Reviews 116:1–16. https://doi.org/10.1016/j.earscirev.2012.10.007, URL https://linkinghub.elsevier.com/retrieve/pii/S0012825212001353

Birnbaum J, Wadsworth FB, Kendrick JE, et al (2026) Disequilibrium response to tapping crustal magma reveals storage conditions. Nature 652(8109):387–392. https://doi.org/10.1038/s41586-026-10317-w, URL https://www.nature.com/articles/s41586-026-10317-w

Blong RJ, Blong RJ (1984) Volcanic hazards: a sourcebook on the effects of eruptions. Academic Press, Sydney Orlando, Fla

Blott SJ, Pye K (2001) GRADISTAT: a grain size distribution and statistics package for the analysis of unconsolidated sediments. Earth Surface Processes and Landforms 26(11):1237–1248. https://doi.org/10.1002/esp.261, URL https://onlinelibrary.wiley.com/doi/10.1002/esp.261

Bursik M, Sieh K, Meltzner A (2014) Deposits of the most recent eruption in the Southern Mono Craters, California: Description, interpretation and implications for regional marker tephras. Journal of Volcanology and Geothermal Research 275:114–131. https://doi.org/10.1016/j.jvolgeores.2014.02.015, URL https://linkinghub.elsevier.com/retrieve/pii/S0377027314000626

Cage AG, Davies SM, Wastegård S, et al (2011) Identification of the Icelandic Landnám tephra (AD 871 ± 2) in Scottish fjordic sediment. Quaternary International 246(1-2):168–176. https://doi.org/10.1016/j.quaint.2011.08.016, URL https://linkinghub.elsevier.com/retrieve/pii/S1040618211004708

Campbell ME, Porritt L, Russell J (2016) Forensic recovery of transient eruption parameters for the 2360BP fall deposit, Mount Meager, British Columbia.

Journal of Volcanology and Geothermal Research 312:11–25. https://doi.org/10.1016/j.jvolgeores.2016.01.013, URL https://linkinghub.elsevier.com/retrieve/pii/S0377027316000238

Cas R, Giordano G, Wright JV (2024) Volcanology: Processes, Deposits, Geology and Resources. Springer Textbooks in Earth Sciences, Geography and Environment, Springer International Publishing, Cham, https://doi.org/10.1007/978-3-319-66613-6, URL https://link.springer.com/10.1007/978-3-319-66613-6

Cassidy M, Manga M, Cashman K, et al (2018) Controls on explosive-effusive volcanic eruption styles. Nature Communications 9(1):2839. https://doi.org/10.1038/s41467-018-05293-3, URL https://www.nature.com/articles/s41467-018-05293-3

Castro J, Walter S (2021) Hybrid rhyolitic eruption at Big Glass Mountain, CA, USA. Volcanica 4(2):257–277. https://doi.org/10.30909/vol.04.02.257277, URL https://www.jvolcanica.org/ojs/index.php/volcanica/article/view/121

Castro JM, Bindeman IN, Tuffen H, et al (2014) Explosive origin of silicic lava: Textural and d D–H2O evidence for pyroclastic degassing during rhyolite effusion. Earth and Planetary Science Letters 405:52–61. https://doi.org/10.1016/j.epsl.2014.08.012, URL https://linkinghub.elsevier.com/retrieve/pii/S0012821X1400510X

Colombier M, Wadsworth FB, Gurioli L, et al (2017) The evolution of pore connectivity in volcanic rocks. Earth and Planetary Science Letters 462:99–109. https://doi.org/10.1016/j.epsl.2017.01.011, URL https://linkinghub.elsevier.com/retrieve/pii/S0012821X17300171

Costa A, Folch A, Macedonio G (2010) A model for wet aggregation of ash particles in volcanic plumes and clouds: 1. Theoretical formulation. Journal of Geophysical Research: Solid Earth 115(B9):2009JB007175. https://doi.org/10.1029/2009JB007175, URL https://agupubs.onlinelibrary.wiley.com/doi/10.1029/2009JB007175

Crozier J, Tramontano S, Forte P, et al (2022) Outgassing through magmatic fractures enables effusive eruption of silicic magma. Journal of Volcanology and Geothermal Research 430:107617. https://doi.org/10.1016/j.jvolgeores.2022.107617, URL https://linkinghub.elsevier.com/retrieve/pii/S0377027322001482

Cáceres F, Wadsworth FB, Scheu B, et al (2020) Can nanolites enhance eruption explosivity? Geology 48(10):997–1001. https://doi.org/10.1130/G47317.1, URL https://pubs.geoscienceworld.org/gsa/geology/article/48/10/997/587448/Can-nanolites-enhance-eruption-explosivity

Degruyter W, Bachmann O, Burgisser A, et al (2012) The effects of outgassing on the transition between effusive and explosive silicic eruptions. Earth and Planetary Science Letters 349-350:161–170. https://doi.org/10.1016/j.epsl.2012.06.056, URL https://linkinghub.elsevier.com/retrieve/pii/S0012821X12003482

Denton J, Tuffen H, Gilbert J (2012) Variations in hydration within perlitised rhyolitic lavas—evidence from Torfajökull, Iceland. Journal of Volcanology and Geothermal Research 223-224:64–73. https://doi.org/10.1016/j.jvolgeores.2012.02.005, URL https://linkinghub.elsevier.com/retrieve/pii/S0377027312000352

Elissondo M, Baumann V, Bonadonna C, et al (2016) Chronology and impact of the 2011 Cordón Caulle eruption, Chile. Natural Hazards and Earth System Sciences 16(3):675–704. https://doi.org/10.5194/nhess-16-675-2016, URL https://nhess.copernicus.org/articles/16/675/2016/

Farquharson JI, Tuffen H, Wadsworth FB, et al (2022) In-conduit capture of sub-micron volcanic ash particles via turbophoresis and sintering. Nature Communications 13(1):4713. https://doi.org/10.1038/s41467-022-32522-7, URL https://www.nature.com/articles/s41467-022-32522-7

Folk RL, Ward WC (1957) Brazos River Bar: A Study in the Significance of Grain Size Parameters. Journal of Sedimentary Research 27(1). https://doi.org/https://doi.org/10.1306/74D70646-2B21-11D7-8648000102C1865D

Gardner JE, Wadsworth FB, Llewellin EW, et al (2019) Experimental constraints on the textures and origin of obsidian pyroclasts. Bulletin of Volcanology 81(4):22. https://doi.org/10.1007/s00445-019-1283-z, URL http://link.springer.com/10.1007/s00445-019-1283-z

Gardner JE, Wadsworth FB, Carley TL, et al (2023) Bubble Formation in Magma. Annual Review of Earth and Planetary Sciences 51(1):annurev–earth–031621–080308. https://doi.org/10.1146/annurev-earth-031621-080308, URL https://www.annualreviews.org/doi/10.1146/annurev-earth-031621-080308

Giachetti T, Gonnermann H (2013) Water in volcanic pyroclast: Rehydration or incomplete degassing? Earth and Planetary Science Letters 369-370:317–332. https://doi.org/10.1016/j.epsl.2013.03.041, URL https://linkinghub.elsevier.com/retrieve/pii/S0012821X13001623

Giachetti T, Druitt T, Burgisser A, et al (2010) Bubble nucleation, growth and coalescence during the 1997 Vulcanian explosions of Soufrière Hills Volcano, Montserrat. Journal of Volcanology and Geothermal Research 193(3-4):215–231. https://doi.org/10.1016/j.jvolgeores.2010.04.001, URL https://linkinghub.elsevier.com/retrieve/pii/S0377027310001162

Giachetti T, Gonnermann HM, Gardner JE, et al (2015) Discriminating secondary from magmatic water in rhyolitic matrix-glass of volcanic pyroclasts using thermogravimetric analysis. Geochimica et Cosmochimica Acta 148:457–476. https://doi.org/10.1016/j.gca.2014.10.017, URL https://linkinghub.elsevier.com/retrieve/pii/S0016703714006255

Giachetti T, Trafton KR, Wiejaczka J, et al (2021) The products of primary magma fragmentation finally revealed by pumice agglomerates. Geology 49(11):1307–1311. https://doi.org/10.1130/G48902.1, URL https://pubs.geoscienceworld.org/geology/article/49/11/1307/606362/The-products-of-primary-magma-fragmentation

Gillies JK, Llewellin EW, Wadsworth FB, et al (2026) Formation of lauoho o Pele (Pele's hair) by extreme stretching of bubbly magma. Geology 54(5):446–450. https://doi.org/10.1130/G53972.1, URL https://pubs.geoscienceworld.org/geology/article/54/5/446/726889/Formation-of-lauoho-o-Pele-Pele-s-hair-by-extreme

Hajimirza S, Gonnermann HM, Gardner JE, et al (2019) Predicting Homogeneous Bubble Nucleation in Rhyolite. Journal of Geophysical Research: Solid Earth 124(3):2395–2416. https://doi.org/10.1029/2018JB015891, URL https://agupubs.onlinelibrary.wiley.com/doi/10.1029/2018JB015891

Hodgetts AGE, Watt SFL, Smith VC, et al (2025) A 400-k.y. perspective on arc volcanism: An exceptional explosive eruption record from Central Mexico. GSA Bulletin 137(11-12):5353–5380

Horwell C, Stannett G, Andronico D, et al (2010) A physico-chemical assessment of the health hazard of Mt. Vesuvius volcanic ash. Journal of Volcanology and Geothermal Research 191(3-4):222–232. https://doi.org/10.1016/j.jvolgeores.2010.01.014, URL https://linkinghub.elsevier.com/retrieve/pii/S0377027310000302

Houghton BF, Carey RJ, Cashman KV, et al (2010) Diverse patterns of ascent, degassing, and eruption of rhyolite magma during the 1.8ka Taupo eruption, New Zealand: Evidence from clast vesicularity. Journal of Volcanology and Geothermal Research 195(1):31–47. https://doi.org/10.1016/j.jvolgeores.2010.06.002, URL https://linkinghub.elsevier.com/retrieve/pii/S0377027310001836

Hoult H, Kennedy BM, Hanson JB, et al (2025) Breaking down walls: conduit wall evolution during explosive activity at an andesitic stratovolcano. Bulletin of Volcanology 87(12):106. https://doi.org/10.1007/s00445-025-01904-2, URL https://link.springer.com/10.1007/s00445-025-01904-2

Iacovino K, Till CB (2019) DensityX: A program for calculating the densities of magmatic liquids up to 1,627 °C and 30 kbar. Volcanica 2(1):1–10. https://doi.org/10.30909/vol.02.01.0110, URL http://jvolcanica.org/ojs/index.php/volcanica/article/view/12

Lara L, Naranjo J, Moreno H (2004) Rhyodacitic fissure eruption in Southern Andes (Cordón Caulle; 40.5°S) after the 1960 (Mw:9.5) Chilean earthquake: a structural interpretation. Journal of Volcanology and Geothermal Research 138(1-2):127–138. https://doi.org/10.1016/j.jvolgeores.2004.06.009, URL https://linkinghub.elsevier.com/retrieve/pii/S0377027304002136

Larsen G (1984) Recent Volcanic History of the Veidivötn Fissure Swarm, Southern Iceland – An Approach to Volcanic Risk Assessment. Journal of Volcanology and Geothermal Research 22, 33-58. https://doi.org/https://doi.org/10.1016/0377-0273(84)90034-9

Liu Y, Zhang Y, Behrens H (2005) Solubility of H2O in rhyolitic melts at low pressures and a new empirical model for mixed H2O–CO2 solubility in rhyolitic melts. Journal of Volcanology and Geothermal Research 143(1-3):219–235. https://doi.org/10.1016/j.jvolgeores.2004.09.019, URL https://linkinghub.elsevier.com/retrieve/pii/S0377027305000442

Llewellin E (2010a) LBflow: An extensible lattice Boltzmann framework for the simulation of geophysical flows. Part I: theory and implementation. Computers & Geosciences 36(2):115–122. https://doi.org/10.1016/j.cageo.2009.08.004, URL https://linkinghub.elsevier.com/retrieve/pii/S0098300409002660

Llewellin E (2010b) LBflow: An extensible lattice Boltzmann framework for the simulation of geophysical flows. Part II: usage and validation. Computers & Geosciences 36(2):123–132. https://doi.org/10.1016/j.cageo.2009.08.003, URL https://linkinghub.elsevier.com/retrieve/pii/S0098300409002659

Loughlin SC, Sparks S, Brown SK, et al (eds) (2015) Global Volcanic Hazards and Risk, 1st edn. Cambridge University Press, https://doi.org/10.1017/CBO9781316276273, URL https://www.cambridge.org/core/product/identifier/9781316276273/type/book

Macdonald R, McGarvie DW, Pinkerton H, et al (1990) Petrogenetic Evolution of the Torfajokull Volcanic Complex, Iceland I. Relationship Between the Magma Types. Journal of Petrology 31(2):429–459. https://doi.org/10.1093/petrology/31.2.429, URL https://academic.oup.com/petrology/article-lookup/doi/10.1093/petrology/31.2.429

Macedonio G, Dobran F, Neri A (1994) Erosion processes in volcanic conduits and application to the AD 79 eruption of Vesuvius. Earth and Planetary Science Letters 121(1-2):137–152. https://doi.org/10.1016/0012-821X(94)90037-X, URL https://linkinghub.elsevier.com/retrieve/pii/0012821X9490037X

McCartney KN, Hammer JE, Shea T, et al (2025) Does Bubble Nucleation Occur Heterogeneously in Magmas Feeding Explosive Rhyolite Eruptions? Insights From the Rock Magnetic Properties of Pumice. Geophysical Research Letters 52(16):e2025GL115789. https://doi.org/10.1029/2025GL115789, URL https://agupubs.onlinelibrary.wiley.com/doi/10.1029/2025GL115789

McGarvie DW (1984) Torfajökull: A volcano dominated by magma mixing. Geology 12(11):685. https://doi.org/10.1130/0091-7613(1984)12<685:TAVDBM>2.0.CO;2, URL https://pubs.geoscienceworld.org/geology/article/12/11/685-688/188337

McGarvie DW, Macdonald R, Pinkerton H (1990) Petrogenetic Evolution of the Torfajokull Volcanic Complex, Iceland II. The Role of Magma Mixing. Journal of Petrology 31(2):461–481

McGarvie, David W. (1985) Volcanology and petrology of mixed magnas and rhyolites from the Torfajokull volcano, Iceland. PhD thesis, University of Lancaster

Miwa T, Geshi N (2012) Decompression rate of magma at fragmentation: Inference from broken crystals in pumice of vulcanian eruption. Journal of Volcanology and Geothermal Research 227-228:76–84. https://doi.org/10.1016/j.jvolgeores.2012.03.003, URL https://linkinghub.elsevier.com/retrieve/pii/S0377027312000662

Owen J, Tuffen H, McGarvie DW (2012) Using dissolved H2O in rhyolitic glasses to estimate palaeo-ice thickness during a subglacial eruption at Bláhnúkur (Torfajökull, Iceland). Bulletin of Volcanology 74(6):1355–1378. https://doi.org/10.1007/s00445-012-0601-5, URL http://link.springer.com/10.1007/s00445-012-0601-5

Owen J, Tuffen H, McGarvie DW (2013a) Explosive subglacial rhyolitic eruptions in Iceland are fuelled by high magmatic H2O and closed-system degassing. Geology 41(2):251–254. https://doi.org/10.1130/G33647.1, URL https://pubs.geoscienceworld.org/geology/article/41/2/251-254/131234

Owen J, Tuffen H, McGarvie DW (2013b) Pre-eruptive volatile content, degassing paths and depressurisation explaining the transition in style at the subglacial rhyolitic eruption of Dalakvísl, South Iceland. Journal of Volcanology and Geothermal Research 258:143–162. https://doi.org/10.1016/j.jvolgeores.2013.03.021, URL https://linkinghub.elsevier.com/retrieve/pii/S0377027313000978

Pallister JS, Diefenbach AK, Burton WC, et al (2013) The Chaitén rhyolite lava dome: Eruption sequence, lava dome volumes, rapid effusion rates and source of the rhyolite magma. Andean Geology 40(2):277–294. https://doi.org/10.5027/andgeoV40n2-a06, URL http://www.andeangeology.cl/index.php/revista1/article/view/2666

Pistolesi M, Cioni R, Bonadonna C, et al (2015) Complex dynamics of small-moderate volcanic events: the example of the 2011 rhyolitic Cordón Caulle eruption, Chile. Bulletin of Volcanology 77(1):3. https://doi.org/10.1007/s00445-014-0898-3, URL http://link.springer.com/10.1007/s00445-014-0898-3

Rust AC, Cashman KV (2007) Multiple origins of obsidian pyroclasts and implications for changes in the dynamics of the 1300 B.P. eruption of Newberry Volcano, USA. Bulletin of Volcanology 69(8):825–845. https://doi.org/10.1007/s00445-006-0111-4, URL http://link.springer.com/10.1007/s00445-006-0111-4

Rust AC, Cashman KV (2011) Permeability controls on expansion and size distributions of pyroclasts. Journal of Geophysical Research: Solid Earth 116(B11):n/a–n/a. https://doi.org/10.1029/2011JB008494, URL http://doi.wiley.com/10.1029/

2011JB008494

Saemundsson K, Larsen G (2019) Torfajökull

Saubin E, Tuffen H, Gurioli L, et al (2016) Conduit Dynamics in Transitional Rhyolitic Activity Recorded by Tuffisite Vein Textures from the 2008–2009 Chaitén Eruption. Frontiers in Earth Science 4. https://doi.org/10.3389/feart.2016.00059, URL http://journal.frontiersin.org/Article/10.3389/feart.2016.00059/abstract

Saubin E, Kennedy B, Tuffen H, et al (2021) Textural and geochemical window into the IDDP-1 rhyolitic melt, Krafla, Iceland, and its reaction to drilling. GSA Bulletin 133(9-10):1815–1830. https://doi.org/10.1130/B35598.1, URL https://pubs.geoscienceworld.org/gsabulletin/article/133/9-10/1815/593788/Textural-and-geochemical-window-into-the-IDDP-1

Schipper CI, Castro JM, Tuffen H, et al (2013) Shallow vent architecture during hybrid explosive–effusive activity at Cordón Caulle (Chile, 2011–12): Evidence from direct observations and pyroclast textures. Journal of Volcanology and Geothermal Research 262:25–37. https://doi.org/10.1016/j.jvolgeores.2013.06.005, URL https://linkinghub.elsevier.com/retrieve/pii/S0377027313001790

Schipper CI, Castro JM, Kennedy BM, et al (2021) Silicic conduits as supersized tuffisites: Clastogenic influences on shifting eruption styles at Cordón Caulle volcano (Chile). Bulletin of Volcanology 83(2):11. https://doi.org/10.1007/s00445-020-01432-1, URL http://link.springer.com/10.1007/s00445-020-01432-1

Schmid MM, Dugmore AJ, Vésteinsson O, et al (2017) Tephra isochrons and chronologies of colonisation. Quaternary Geochronology 40:56–66. https://doi.org/10.1016/j.quageo.2016.08.002, URL https://linkinghub.elsevier.com/retrieve/pii/S1871101416301029

Shea T (2017) Bubble nucleation in magmas: A dominantly heterogeneous process? Journal of Volcanology and Geothermal Research 343:155–170. https://doi.org/10.1016/j.jvolgeores.2017.06.025, URL https://linkinghub.elsevier.com/retrieve/pii/S0377027317302688

Shea T, Houghton BF, Gurioli L, et al (2010) Textural studies of vesicles in volcanic rocks: An integrated methodology. Journal of Volcanology and Geothermal Research 190(3-4):271–289. https://doi.org/10.1016/j.jvolgeores.2009.12.003, URL https://linkinghub.elsevier.com/retrieve/pii/S0377027309004624

Shields J, Mader H, Caricchi L, et al (2016) Unravelling textural heterogeneity in obsidian: Shear-induced outgassing in the Rocche Rosse flow. Journal of Volcanology and Geothermal Research 310:137–158. https://doi.org/10.1016/j.jvolgeores.2015.12.003, URL https://linkinghub.elsevier.com/retrieve/pii/S0377027315004096

Singer BS, Jicha BR, Harper MA, et al (2008) Eruptive history, geochronology, and magmatic evolution of the Puyehue-Cordon Caulle volcanic complex, Chile. Geological Society of America Bulletin 120(5-6):599–618. https://doi.org/10.1130/B26276.1, URL https://pubs.geoscienceworld.org/gsabulletin/article/120/5-6/599-618/2277

Toramaru A (2006) BND (bubble number density) decompression rate meter for explosive volcanic eruptions. Journal of Volcanology and Geothermal Research 154(3-4):303–316. https://doi.org/10.1016/j.jvolgeores.2006.03.027, URL https://linkinghub.elsevier.com/retrieve/pii/S0377027306001363

Trafton KR, Giachetti T (2022) The pivotal role of Vulcanian activity in ending the explosive phase of rhyolitic eruptions: the case of the Big Obsidian Flow eruption (Newberry Volcano, USA). Bulletin of Volcanology 84(12):104. https://doi.org/10.1007/s00445-022-01610-3, URL https://link.springer.com/10.1007/s00445-022-01610-3

Tuffen H, McGarvie DW, Pinkerton H, et al (2008) An explosive–intrusive subglacial rhyolite eruption at Dalakvísl, Torfajökull, Iceland. Bulletin of Volcanology 70(7):841–860. https://doi.org/10.1007/s00445-007-0174-x, URL http://link.springer.com/10.1007/s00445-007-0174-x

Unwin HE, Tuffen H, Phillips E, et al (2021) Pressure-Driven Opening and Filling of a Volcanic Hydrofracture Recorded by Tuffisite at Húsafell, Iceland: A Potential Seismic Source. Frontiers in Earth Science 9:668058. https://doi.org/10.3389/feart.2021.668058, URL https://www.frontiersin.org/articles/10.3389/feart.2021.668058/full

Vasseur J, Wadsworth FB, Dingwell DB (2020) Permeability of polydisperse magma foam. Geology 48(6):536–540. https://doi.org/10.1130/G47094.1, URL https://pubs.geoscienceworld.org/gsa/geology/article/48/6/536/583181/Permeability-of-polydisperse-magma-foam

Wadsworth FB, Llewellin EW, Vasseur J, et al (2020) Explosive-effusive volcanic eruption transitions caused by sintering. Science Advances 6(39):eaba7940. https://doi.org/10.1126/sciadv.aba7940, URL https://www.science.org/doi/10.1126/sciadv.aba7940

Wadsworth FB, Llewellin EW, Castro JM, et al (2022) A reappraisal of explosive–effusive silicic eruption dynamics: syn-eruptive assembly of lava from the products of cryptic fragmentation. Journal of Volcanology and Geothermal Research 432:107672. https://doi.org/10.1016/j.jvolgeores.2022.107672, URL https://linkinghub.elsevier.com/retrieve/pii/S0377027322002037

Walker GPL (1973) Explosive volcanic eruptions — a new classification scheme. Geologische Rundschau 62(2):431–446. https://doi.org/10.1007/BF01840108, URL http://link.springer.com/10.1007/BF01840108

Watt SFL, Pyle DM, Mather TA, et al (2009) Fallout and distribution of volcanic ash over Argentina following the May 2008 explosive eruption of Chaitén, Chile. Journal of Geophysical Research: Solid Earth 114(B4):2008JB006219. https://doi.org/10.1029/2008JB006219, URL https://agupubs.onlinelibrary.wiley.com/doi/10.1029/2008JB006219

White JD, Valentine GA (2016) Magmatic versus phreatomagmatic fragmentation: Absence of evidence is not evidence of absence. Geosphere 12(5):1478–1488. https://doi.org/10.1130/GES01337.1, URL https://pubs.geoscienceworld.org/geosphere/article/12/5/1478-1488/189705

Zhang J, Tuffen H, Wadsworth FB, et al (2026) Sustained ash emission during lava effusion is a hidden volcanic hazard of silicic eruptions. Nature Communications https://doi.org/10.1038/s41467-026-76464-w, URL https://www.nature.com/articles/s41467-026-76464-w

Zimanowski B, Büttner R, Dellino P, et al (2015) Magma–Water Interaction and Phreatomagmatic Fragmentation. In: The Encyclopedia of Volcanoes. Elsevier, p 473–484, https://doi.org/10.1016/B978-0-12-385938-9.00026-2, URL https://linkinghub.elsevier.com/retrieve/pii/B9780123859389000262

Supplementary Files

This is a list of supplementary files associated with this preprint. Click to download.

- bulvolctephrasupplementaryver1260911.docx
- bulvolctephrasupplementaryver1.xlsx